University of Seville
Master in Nuclear Physics

Characterisation of a pure LaCl₃-based detector for proton therapy application

Georgina Xifra Goya

17th July 2023

Supervisors:

Enrique Nácher González

Marcos Martínez Roig

University supervisor:

Manuel García León

Abstract

Proton therapy is an increasingly used technique for cancer treatment worldwide. However, the uncertainty in proton range verification requires the use of wide safety margins in proton doses, limiting its full potential. This project aims to test the feasibility of using a pure $LaCl_3$ scintillator, in coaxial configuration with a proton beam. The goal is to determine the position of the Bragg peak with a substantial improvement in its spatial uncertainty by detecting the gamma-rays and neutrons emerging from the patients. The concept relies on the solid angle effect, where closer sources result in higher counting rates in the detector. Pure $LaCl_3$ scintillators, currently not available in the market, offer excellent discrimination between neutrons and gamma-rays, surpassing the limitations of current detectors. Moreover, they enable double real-time verification of the proton range. To assess the sensitivity of the pure $LaCl_3$ detector, several studies have been conducted aiming to measure the variation in the count rate in response to millimetre-scale displacements of the Bragg peak.

Resumen

La protonterapia es una técnica cada vez más utilizada para el tratamiento del cáncer. Sin embargo, la incertidumbre en la verificación del rango de los protones implica la necesidad de utilitzar ámplios márgenes de seguridad en las dosis, limitando su potencial total. Este proyecto tiene como objetivo comprobar la viabilidad del uso de un centelleador de $LaCl_3$ puro, en configuración coaxial con un haz de protones. Se busca determinar la posición del pico de Bragg, con una mejora sustancial en su incertidumbre espacial, mediante la detección de los rayos gamma y neutrones emitidos por los pacientes. El concepto se basa en el efecto del ángulo sólido, donde las fuentes más cercanas resultan en mayores tasas de conteo en el detector. Los centelladores de $LaCl_3$ puro, que no se encuentran actualmente en el mercado, ofrecen una excelente discriminación entre neutrones y rayos gamma, superando las limitaciones de los detectores actuales. Además, permiten la doble verificación en tiempo real del rango de protones. Para evaluar la sensibilidad del detector de $LaCl_3$ puro, se han llevado a cabo varios estudios donde se pretende medir la variación en la tasa de cuentas ante desplazamientos milimétricos del pico de Bragg.

Acknowledgements

I would like to express my gratitude to my two thesis supervisors, Enrique Nácher González and Marcos Martínez Roig. Their invaluable mentorship, expertise, and unwavering support have been crucial to the successful completion of my thesis.

I feel compelled to thank, once again, Phan Quoc Vuong and Hongjoo Kim from the Department of Physics at Kyungpook National University for letting us have the privilege to study a non commercial pure $LaCl_3$ scintillator to conduct my master thesis and develop the PRIDE project.

I wish to extend my appreciation to my parents and brother for their encouragement in pursuing my dreams from a young age, as well as their continuous support throughout my bachelor's and master's studies.

I would like to express my heartfelt gratitude to my friends for their ability to understand my limited availability and provide me with much-needed moments of disconnection when necessary.

I would also like to thank my partner for his encouragement, understanding, and valuable insights during this journey.

Thank you all for being there with me.

Contents

1   Introduction

In recent years, proton therapy has emerged as a promising technique for cancer treatment, offering precise targeting of tumours while minimising damage to surrounding healthy tissues. It is possible to accurately control the radiation dose deposition inside the patient's body thanks to the inherent physical properties of the protons. Nonetheless, precise range verification is crucial to maximise the potential of proton therapy. It involves verifying the depth of proton penetration in tissue to guarantee both treatment effectiveness and patient security. Therefore, the ability to verify the range of protons in real-time plays a vital role.

Proton therapy is a technique employed for the treatment of cancerous tissue by using proton beams instead of X-rays, distinguishing it from conventional radiotherapy. In order to fully leverage the benefits of proton therapy over traditional X-ray therapy, precise positioning of the Bragg peak within the entire tumour being treated is crucial [1].

The use of charged particles allows to deposit the maximum amount of energy at the end of the trajectory of the particles, which is known as the Bragg peak. The position of this peak depends on the beam's initial energy. One major advantage of protons is having a sharp Bragg peak and a distal falloff near their maximum penetration depth. This enables the precise targeting of the maximum dose at a specific location, resulting in an impact on the cancerous tissue while minimising the effect on the surrounding healthy tissue. Fig. 1 shows the dose profile with the penetration depth of protons and photons in water into the tumour region.
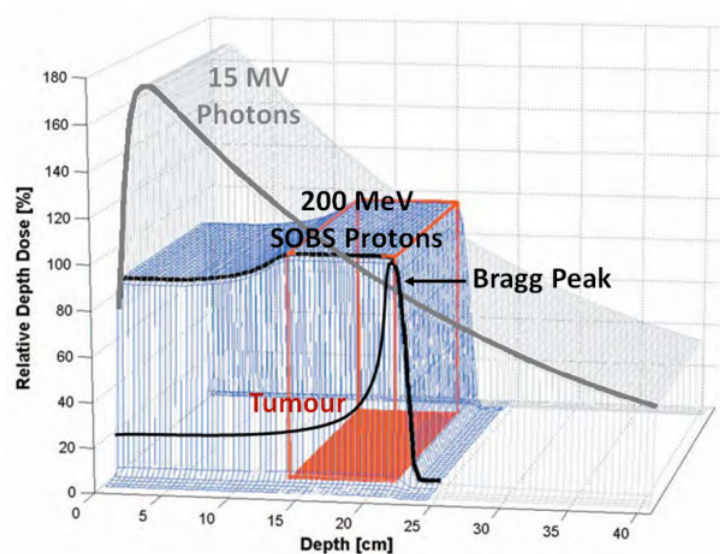

Fig. 1. Comparison between deposited dose as a function of the penetration depth for different initial beam energy for photons and protons. Image taken from reference [2].

Traditional X-ray radiotherapy has a higher chance of damaging the healthy tissue surrounding the affected area since they deposit the maximum dose at shallower depths. As they penetrate further, the dose decreases gradually until the X-rays lose all their energy or, ultimately, exit the body.

Because of having a far higher selectivity than traditional radiotherapy, proton therapy may be a very good alternative for treating tumours in anatomically sensitive regions like the brain or spinal cord.

To ensure the safety and success of the treatment, it is essential to continuously monitor the therapy by verifying the position of the Bragg peak. This can be achieved by measuring, in real-time, the spatial distribution of the dose. No accepted standard or commercial technique is currently used in all proton treatment facilities for proton range verification. Hence, when devising the treatment plan, prudent safety margins are implemented for the proton dosage.

The main goal of this work is to test a detector, to be used in coaxial configuration with the proton beam, to infer the position of the Bragg peak from the detection of γ-rays and neutrons emerging from the patient. The method was proposed theoretically in [3], for the particular case of γ-rays, and it is based on the solid angle effect: the closer the emitting source (in this case the Bragg peak), the higher the counting rate in the detector. We want to follow the same approach but making use of the simultaneous detection of γ-rays and neutrons. Therefore, we need a scintillating crystal, in coaxial configuration, with a good Pulse-Shape Discrimination (PSD) of γ-rays and neutrons, also known as neutron-γ discrimination.

CLYC scintillators (Cs_2LiYCl_6), are widely used and commercialised due to their advantageous features. First of all, their have a good neutron-γ discrimination due to their PSD capability. CLYC detectors also have other notable features such as high efficiency for γ-rays and neutrons, excellent resolution, compact size and low sensitivity to temperature and humidity. Although CLYC scintillators offer advantages, they cannot discriminate between the reaction products within the crystal. The detection of fast neutrons, as well as the discrimination of (n,p) and (n,α) reactions in the crystal, are valuable features exhibited by other scintillators as further explained.

Nowadays, La-halide scintillators, are commercially accessible. They have proven to be highly effective in the field of radiation measurement, especially in low energy nuclear spectroscopy experiments. Since Lanthanum has a high atomic number (Z=57), combined with a high density of the crystal, such as the one of $LaCl_3$, $\rho = 3.85$ g/cm^3, could permit to detect high-energy γ-rays. Nonetheless, La-halide detectors have a self-activity which reduces the detector sensitivity [4], and it can be activated in presence of a radioactive

background.

Currently, LaCl$_3$ can only be commercially found doped with cerium (LaCl$_3$:Ce). This scintillator shares similar characteristics with CLYC. Their properties have been thoroughly studied in [4]. Ce-doped lanthanum scintillators offer an outstanding trade-off between efficiency, energy resolution (3.3% FWHM at 662 keV) and light yield (50 photons/keV). These values are the ones corresponding to commercially optimised cerium doping levels [5]. With their sub-nanosecond time resolution, LaCl$_3$:Ce detectors have the potential to serve as a viable alternative to HPGe detectors for γ-ray studies, as stated in [6]. The exceptional time-of-flight measurement, enabled by the sub-nanosecond time resolution, is typically utilised for discriminating between neutrons and γ-rays and for rejecting background signals. The concentration of cerium also plays an important role regarding PSD. At higher concentrations of cerium, the energy resolution improves to the expense of the PSD discrimination. When decreasing the concentration, the PSD discrimination gets better. Due to the improvement in PSD with the decrease in cerium doping, we could wonder if using pure LaCl$_3$, that is, eliminating the doping, could yield better results. However, pure LaCl$_3$ crystals are not commercially available yet.

Pure LaCl$_3$ offers one of the finest neutron-γ PSD capabilities of any of them, including the CLYC and the Ce-doped LaCl$_3$ scintillators, according to [5]. This is achieved at the cost of getting reduced values of light yield (34 photons/keV), energy resolution (4.7% FWHM at 662 keV) and a slower decay than Ce-doped ones [7].

Apart from obtaining and excellent PSD discrimination, we could also do neutron spectroscopy using pure LaCl$_3$ crystals, since this scintillator is able to discriminate between proton and α-particles. It is viable because fast neutrons react with ^{35}Cl isotope, the richest concentration of isotope present in the crystal, through two reactions with a significant cross-section:^{35}Cl(n,p)^{35}S and ^{35}Cl(n,α)^{32}P [8].

Up-to-date, several solutions have been proposed for real-time range verification problems. We want to propose pure LaCl$_3$ crystals in coaxial configuration for proton range verification, due to their neutron-γ separation, the optimum energy resolution, and the time response [5]. Proton range verification is the key aspect to reduce the margins of uncertainty introduced in proton therapy treatments, such as the uncertainty on the exact position of the Bragg peak.

2　Motivation and objectives

The interest in investigating a non-commercial pure $LaCl_3$ scintillator arose from its potential applications in proton therapy due to its promising capability for PSD.

We were able to obtain the pure $LaCl_3$ scintillating crystal thanks to Phan Quoc Vuong and Hongjoo Kim from the Department of Physics at Kyungpook National University [5]. Their kind offer allowed us to conduct tests on the scintillator in a coaxial mode at different accelerator facilities.

This Master's thesis aims to study a small pure $LaCl_3$ crystal, coaxial to the proton beam, within the context of the PRIDE project (Proton Range and Imaging DEvice), specifically focusing on its potential for γ-neutron discrimination by PSD. It consists of building a novel scanner capable of solving the current problems of range verification in proton therapy in a single device that can integrate new methods for p-CT (Proton-Computed Tomography) [9] and p-RV (Proton Range Verification).

The goal of investigating pure $LaCl_3$ is to identify the optimal configuration parameters for the detector to achieve the most effective differentiation between γ-rays and neutrons. Additionally, if feasible, the aim is to discern the reaction products of neutrons within the crystal, such as α-particles and protons, allowing us to perform spectroscopy. Once the parameters are determined, the next step is to validate the setup by testing it with an energetic beam and comparing the obtained results with the simulated outcomes.

3　Methodology and content development

We must construct a prototype of a coaxial detector based on the assembly of the pure $LaCl_3$ crystal and a Photo-Multiplier Tube (PMT), as we can see in Fig. 2 to evaluate the PSD capability of a pure $LaCl_3$ scintillator. With the Hamamatsu model R1924A-700, we will conduct a thorough analysis of the PMT parameters. We will also examine the results of switching the PMT to a Hamamatsu model R6233-100, which has a slower time response to PSD discrimination.

The scintillator has a truncated conical shape, measuring 16 mm in height, with a larger diameter of 22.5 mm and a smaller diameter of 16 mm. Due to having an hygroscopic nature, it is coated with a 2 mm thick layer of polytetrafluoroethylene (PTFE), commonly known as Teflon, and 0.1 mm of aluminium shielding in all the surfaces except the one that connects to the PMT. The side with a larger diameter has a quartz window, specifically borosilicate glass, known for its excellent photon transmission properties (T=99.8% at $\lambda = 435$ nm, measured in ICMOL laboratory).

We coupled the crystal to the PMT using an optical grease 631 from Saint-Gobain Crystals, Fig. 2b. To ensure a correct coupling and precise alignment, we designed a black cover using 3D printing, shown in Fig. 2c, which also works to improve its opacity. Once the coupling was complete, we used black adhesive tape to prevent light from entering our device, as depicted in Fig. 2d.
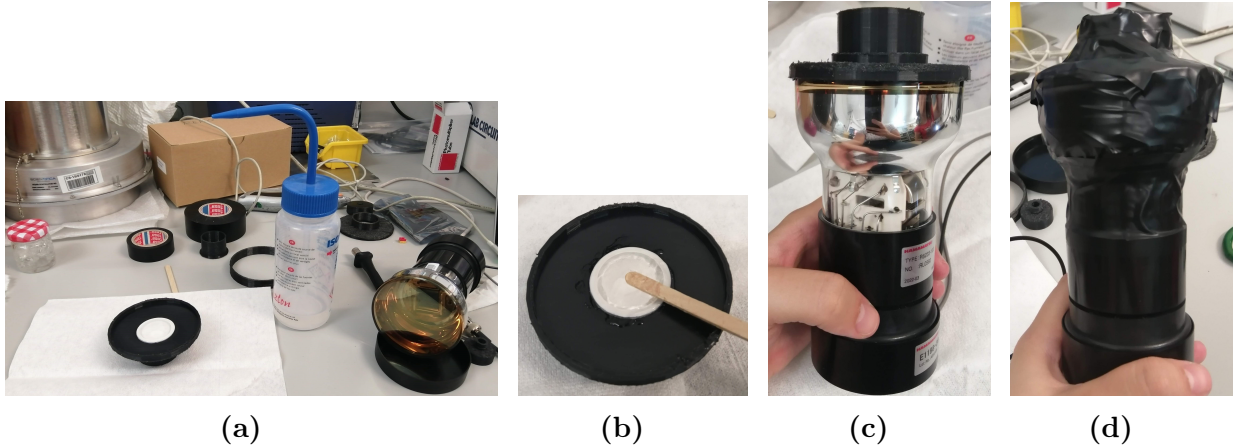

(a)   (b)   (c)   (d)

Fig. 2. Steps followed to make the assembly of the detector parts with the Hamamatsu model: R6233-100. From left to right: a) All the detector parts before assembly, b) Optical coupling applied, c) Scintillator and PMT coupled, d) Assembly finished.

The same procedure has been followed to couple the Hamamatsu R1924A-700 PMT to the scintillator and study its effect. In both cases, the module CAEN N1471A provide the high voltage (HV) supply to the PMT and its output signals are digitised using the CAEN DT5725S digitiser.

We will conduct the study of the scintillator's PSD discrimination through a three-phase approach. In the initial phase (at the IFIC laboratory), we will use a ^{252}Cf source to fine-tune the parameters of the detector, including gate lengths and threshold settings. Subsequently, we will make use of the Geant4 simulation package [10] to predict the behaviour of the scintillator using a higher-energy proton source. Finally, we will carry out the conclusive experiment at CMAM, using a 10 MeV proton beam. All the data obtained from these experiments will be analysed using the ROOT data analysis framework.
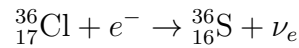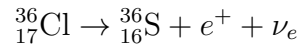
4 Testing the LaCl$_3$ with two different PMTs

4.1 Composition of the pure LaCl$_3$ scintillator

Pure LaCl$_3$ is a ionic crystal composed of lanthanum cations (La^{3+}) and chloride anions (Cl$^-$). Chloride ions (Cl$^-$) exhibit two stable isotopes, $^{35}_{17}$Cl (75.76%) and $^{37}_{17}$Cl (24.24%). On the other hand, the lanthanum cation (La^{3+}) is composed solely of $^{139}_{57}$La stable isotope (99.91%) [11].

Regarding Cl$^-$, we know that $^{35}_{17}$Cl isotope is used to detect neutrons with the (n,p) and (n, α) reactions. Additionally, LaCl$_3$ crystal has also traces of an unstable isotope, $^{36}_{17}$Cl, whose concentration can be increased through neutron capture of $^{35}_{17}$Cl,

$$^{35}_{17}\text{Cl} + n \rightarrow {}^{36}_{17}\text{Cl} + \gamma.$$
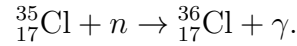
The presence of $^{36}_{17}$Cl can lead to electron capture or decay into $\beta^\pm$, contributing to the background within our detector.

$$^{36}_{17}\text{Cl} \rightarrow {}^{36}_{18}\text{Ar} + e^- + \bar{\nu}_e$$

$$^{36}_{17}\text{Cl} \rightarrow {}^{36}_{16}\text{S} + e^+ + \nu_e$$

$$^{36}_{17}\text{Cl} + e^- \rightarrow {}^{36}_{16}\text{S} + \nu_e$$

In turn, La^{3+} can produce $^{140}_{57}$La by neutron capture,

$$^{139}_{57}\text{La} + n \rightarrow {}^{140}_{57}\text{La} + \gamma.$$
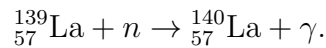
Despite its low energy, this γ-ray contributes to the background. In addition, $^{140}_{57}$La can decay into an excited state of $^{140}_{58}$Ce*,

$$^{140}_{57}\text{La} \rightarrow {}^{140}_{58}\text{Ce}^* + e^- + \bar{\nu}_e$$
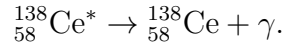
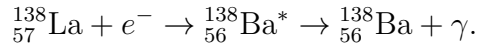producing an additional background under radioactive environment.

LaCl$_3$ scintillator has also $^{138}_{57}$La, a radioactive unstable isotope, which makes up about 0.09% of its naturally occurring form. It decays through,

$$^{138}_{57}\text{La} \rightarrow {}^{138}_{58}\text{Ce}^* + e^- + \bar{\nu}_e$$

into a $^{138}_{58}\text{Ce}^*$, in an excited state, which emits a γ-ray of 778.7 keV,

$$^{138}_{58}\text{Ce}^* \rightarrow {}^{138}_{58}\text{Ce} + \gamma.$$

Another γ-ray of 1435.8 keV is emitted by $^{138}_{57}\text{La}$ through electron capture,

$$^{138}_{57}\text{La} + e^- \rightarrow {}^{138}_{56}\text{Ba}^* \rightarrow {}^{138}_{56}\text{Ba} + \gamma.$$

Apart from the main components of the crystal, actinium is also present in any piece of LaCl$_3$ as a contaminant. This is due to its chemical similarity to lanthanum, since both are located in the same column of the periodic table, making their separation challenging. For a considerable time, actinium alpha contamination involving lanthanum has been a persistent issue [12].

The longest-lived radioactive actinium isotope, ^{227}Ac has a half-life of 21.772 years and is part of the ^{235}U decay series to the stable ^{207}Pb. [13]. It emits α-particles through:

$$^{227}_{89}\text{Ac} \rightarrow {}^{223}_{87}\text{Fr} + \alpha$$
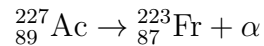
at a rate of 1-2 counts/cm^3 for energies from 5 to 7 MeV. We measure them in the 1.7 to 3 MeV range, due to the alpha pulse deficit [8].

4.2   Digitiser main features

We will use a compact digitiser, the CAEN DT5725S model, in place of the conventional analogue chain to make the data acquisition. We will also employ the CAEN CoMPASS software which enables us to define a number of parameters and carry out an analysis *on-line*.

There are two well-known techniques for triggering the acquisition of pulses: digital leading edge and constant fraction discrimination. The former detects the pulse when the event crosses a predetermined threshold value, while the latter initiates the signal when the input reaches a specific percentage of the total amplitude (f), having a better timing information.

Once the acquisition is triggered, it works like a QDC (Charge to Digital Converter). It has two programmable gates: the long or delayed gate (Q_D), which is used for spectroscopy, and the short or prompt gate (Q_P), which is used for PSD.
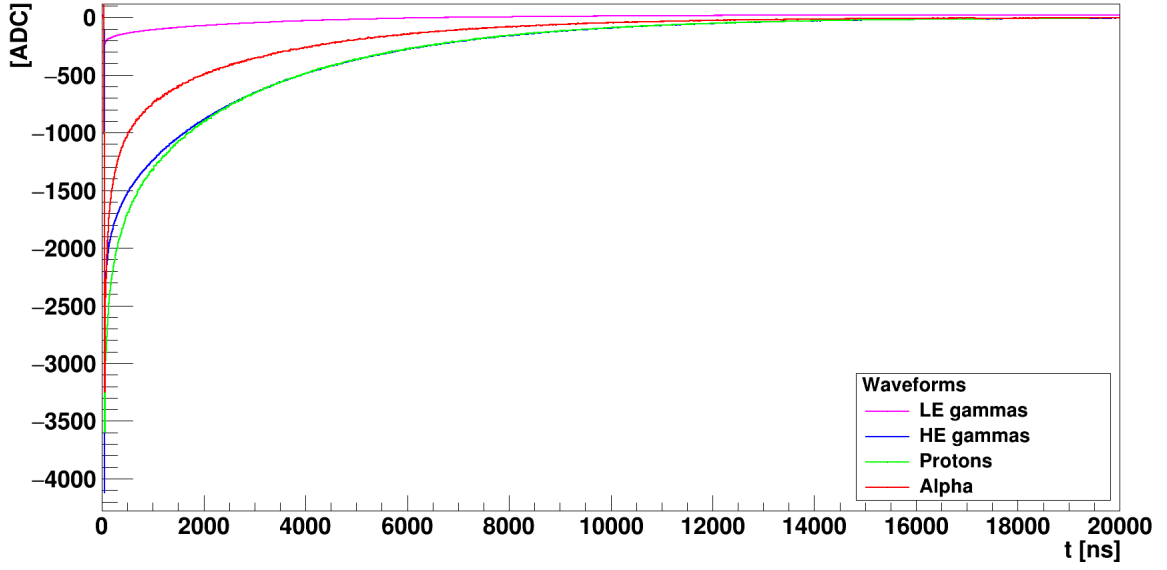
(a)
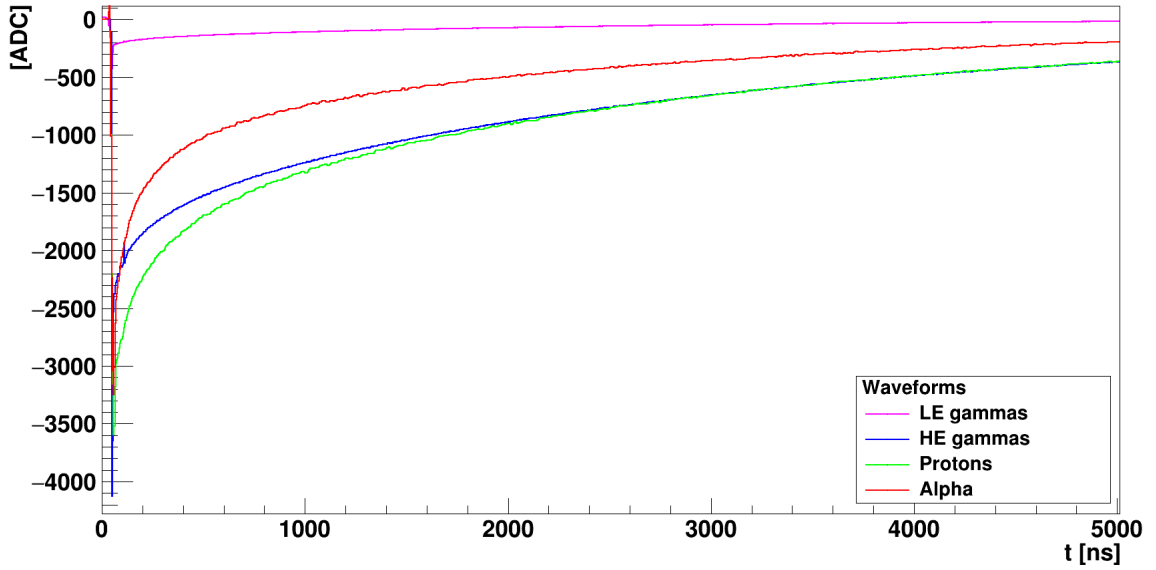
(b)

Fig. 3. **(a)** Waveform plot illustrating the charge response captured by a QDC for γ-rays, protons and α-particles. The y-axis represents the voltage of the signal without calibration to volts (V). **(b)** Zoom of (a), to emphasise the difference in the alpha and proton signals.

This PSD ratio is defined as the difference between the total accumulated charge in the delayed gate and the charge in the prompt gate. This allows us to discriminate particle types based on the PSD ratio, defined as,

$$\text{PSD} = \frac{Q_\text{D} - Q_\text{P}}{Q_\text{D}}. \tag{1}$$

11

The PSD ratio will be very different for different particles detected since they produce different signals (different time response) in the detector+PMT system. In Fig. 3, we can see a comparison of the electronic signals produced for γ-rays of high and low energy, protons and α-particles.
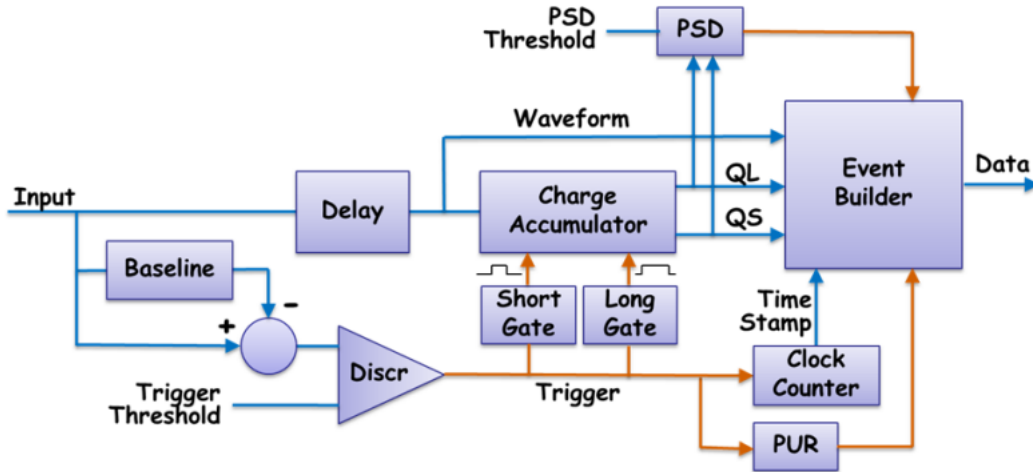

Fig. 4. Diagram of the operational system of the DPP-PSD (Digital Pulse Processing-Pulse Shape Discrimination) [14].

Fig. 4 diagram illustrates the CAEN digitiser's basic working principle. One of the most relevant parameters is the baseline value, which is used as a reference value for the charge integration of the input pulses and other parameters such as the threshold. With the digitiser, we can fix its value or let the software calculate it dynamically.

When working with the PSD algorithm, we want to separate correctly the fast and slow components of the light emitted by the detector. The fast component has a length of a few tens of ns, while the slow one, with a longer tail and a smaller amplitude, has a length of a few μs. The CAEN firmware is designed to register fast signals, giving us a good energy resolution for the fast component. During the time of integration a second pulse might come to the digitiser and therefore, pile-up could occur. It consists of two signals that cross the threshold within the same integration gate. The DAQ takes into account the pile-up and saturation and allows its correction using the dead time. The pile-up events were always kept below 2% of the total.

4.3 First test at the IFIC laboratory

After coupling the scintillator crystal with the PMT, it is necessary to test the detector with a radioactive source of interest in order to optimise its response. This test can be performed in a dark camera with a weak source. Since the interest of this detector is to be able to obtain a good discrimination between neutrons and γ-rays, it is necessary to

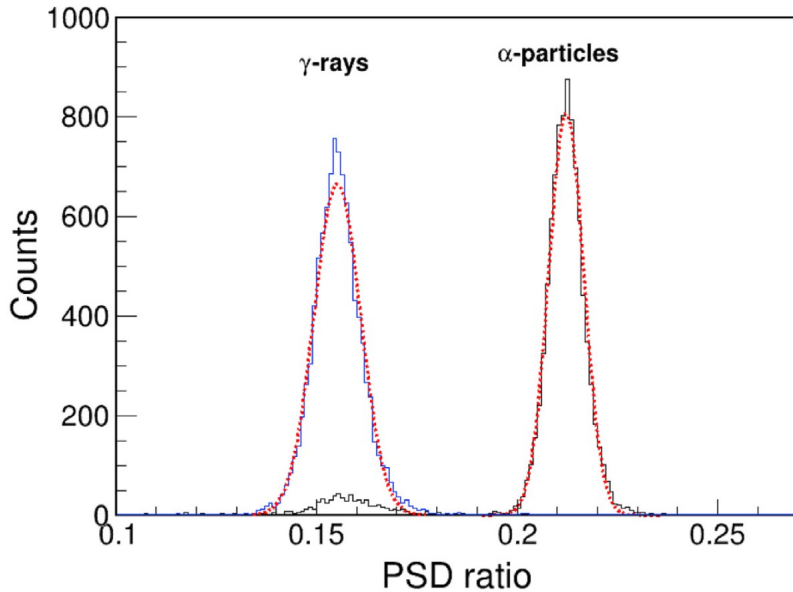use a neutron source. In our case ^{252}Cf, with an activity of approximately 200 Bq.

Fig. 5. PSD spectrum where we can see clearly the separation between the two peaks in the PSD ratio. In this plot the PSD is defined as PSD=$Q_P/(Q_P + Q_D)$. Image taken from [5].

Our main objective is to optimise the separation between the two peaks in the PSD ratio, as shown in Fig. 5.

To do so, we defined the Figure of Merit (FOM) to measure the separation between two peaks in the PSD projection on the x-axis. We define it as the difference between the mean values of the two adjusted Gaussian functions representing the each peak, the alpha peak and the gamma peak, divided by the sum of their respective peak widths (FWHM):

$$\text{FOM} = \frac{|M_\alpha - M_\gamma|}{\text{FWHM}_\alpha + \text{FWHM}_\gamma}.$$ (2)

As we can see, FOM is defined positive.

In order to consider a detector's PSD value acceptable to discriminate two particle types, it is typically required a FOM α/γ value higher than 1.5 [5]. The optimal FOM values achieved using LaCl$_3$ are usually around 2.5.

4.3.1 Fine-tuning the digitiser parameters

Fine-tuning the CoMPASS configuration parameters is essential in order to achieve a high FOM value and therefore, a good PSD discrimination. The configuration parameters, depicted in Fig. 4, have a crucial role to play in this process.

Input		Discriminator		QDC	
Record length	14975 ns	**Mode**	leading edge	**Gain**	160 fC/(LSBxVpp) 40 fC/(LSBxVpp)
Pre-trigger	192 ns	**Threshold**	100 LSB 25 LSB	**Gate**	10000 ns
Polarisation	Neg.	**Trigger holdoff**	1024 ns	**Short gate**	200 ns
N samples baseline	256	**CFD delay**	4 ns	**Pre-gate**	100 ns
Fixed baseline value	0	**CFD fraction**	75%	**Charge pedestal**	1024 LSB
DC offset	20%	**Input Smooth**	Disabled		
Vpp	0.5 V				

Tab. 1. Parameters selected for the R1924A-700 PMT with a HV of -900 V. In blue, the parameters that change when exchanging the PMT for the 6233-100 model. The parameters that change with the HV are the long and short gates and with each PMT, the gain.

Tab. 1 presents the optimised values for these parameters, categorised into input, discriminator, and QDC (Charge-to-Digital Converter). Additionally, Fig. 6 illustrates some of the gathered parameters.

In the input category, there are parameters regarding the input of the signal. Initially, the record length refers to the fixed length within the visually defined acquisition window. The pre-trigger refers to a specific portion of a recorded signal that is captured before the triggering event. The polarisation must be the one that the PMT supports, in this case, negative. We have chosen to calculate the baseline dynamically, adjusting the number of samples at which the baseline is recalculated with the N samples baseline parameter. Thus, the fixed baseline value is equal to zero. The DC offset serves for the adjustment of the baseline voltage level of the captured signal. It is useful when there is a significant DC component, covering the full width of the pulse of the waveform within the dynamic range. It is expressed as the percentage of the full-scale range. Vpp voltage from peak-to-peak, quantifies the amplitude or voltage range of the captured signal.
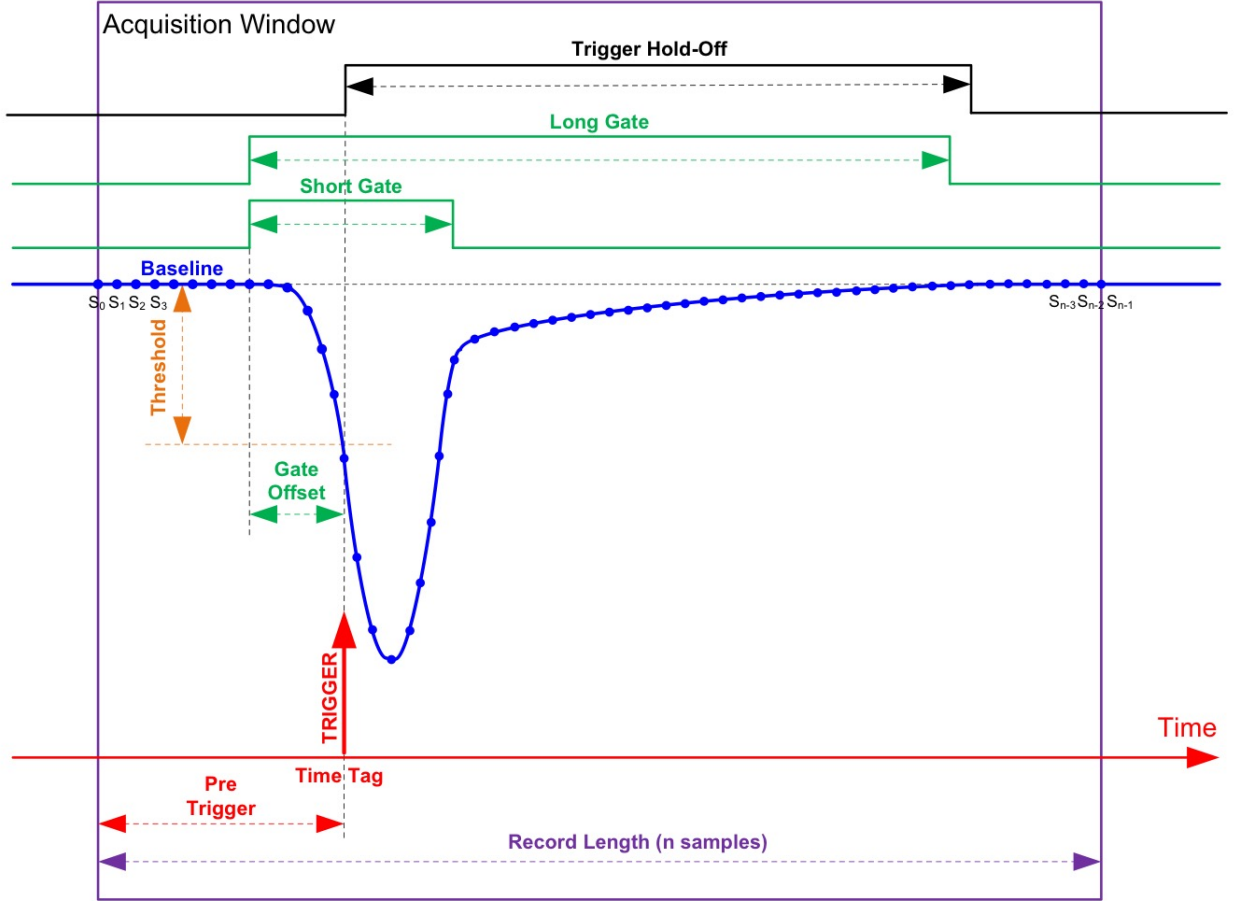
Fig. 6. Diagram that represents the DPP-PSD parameters previously explained for one acquisition window. Picture taken from the User Manual UM5960 of CoMPASS, "Multiparametric DAQ Software for Physics Applications".

In the discriminator section, there is firstly the choice of the triggering acquisition of pulses mode. We have chosen leading edge. There is also the threshold and the trigger holdoff, which is the period of time after the trigger that the system inhibits triggering again. The parameters regarding the constant fraction discrimination (CFD) do not affect when choosing leading edge. Finally, the input smooth is to reduce the fluctuations in the signal, if necessary, in order to enhance the visualisation of the signal profile.

In the charge-to-digital converter (QDC) section, there are parameters regarding the charge integration gates. The gain allows to reescale the signal charge, a uselful feature to adjust the signal to the full-scale range. The gain units are fC/(LSBxVpp), where fC are femtocoulombs, LSB (Least Significant Bit) can be converted to volts using 1 LSB= Vpp/2^{Nbit} conversion. The pre-gate is a parameter that sets the starting position of the gate and short gate before the trigger signal. The short and long gates values are the ones that refer to the charge integration. The charge pedestral is set by default and it is useful for energies close to zero.

To analyse the effect of varying the short gate value on the FOM value, we need to plot the PSD ratio spectrum. Ideally, we should observe distinct peaks corresponding to γ-rays and α-particles. In an optimal scenario, we might even observe an additional peak corresponding to protons. Using the ^{252}Cf weak source and considering our current counting rate, we will determine the optimal values by adjusting the peaks of α-particles and γ-rays and calculating the FOM value. In the following, I will show this analysis and FOM optimisation for each particular PMT.

4.4 HAMAMATSU PMT: R1924A-700

In order to select the desired data, we can generate a plot of PSD vs Energy in the ROOT framework and then apply cuts on the data points corresponding to α-particles and γ-rays. There are two primary approaches to accomplish this: TCutG and energy cuts.

On the one hand, the TCutG method allows us to define a region of interest on the plot by graphically selecting a list of points. This region can encompass the specific range of energies associated with the α-particles and γ-rays, effectively isolating them from the rest of the data. On the other hand, the energy cuts method is more straight-forward because it involves setting vertical boundaries on the energy axis to isolate and visualise the γ-rays and α-particles distinctly, filtering out noise or data below a certain energy value.

Both methods offer different ways to select and analyse the desired data points, enabling us to focus on the α-particles and γ-rays in our study. It is important to mention that calibration was not applied in this case because any modifications to the gate values (prompt and delayed) and the HV directly affect the calibration. Therefore, calibration should be performed once the exploration of optimal parameters to achieve the best FOM is completed.

We have calibrated the gate parameters using three different high voltage supply values (-900 V, -1000 V, and -1100 V) for the PMT. We selected these values based on the PMT specifications, considering the maximum voltage allowed (-1200 V) between the anode and cathode of the PMT.

We observed the PMT signals in the "Waves" mode of the digitalizer, which functions as an oscilloscope, for each high voltage setting. During this analysis, we determined that the valid ranges for integrating the signal's descent are between a short gate of 200 ns, which precisely aligns with the point before the tail begins, and 500 ns. To explore the impact of different short gate values, we tested four options: 200 ns, 300 ns, 400 ns, and 500 ns.

As the voltage increases, both the integrated charge and the total length of the signal

increase, thereby affecting the delayed gate. Consequently, the optimal gate parameters may vary for each voltage value. In the "Waves" mode, we were able to adjust the delayed gate values for each voltage, as demonstrated in Tab. 2.

HV (V)	Short gate (ns)				Delayed gate (ns)
-900	200	300	400	500	12000
-1000	200	300	400	500	14000
-1100	200	300	400	500	16000

Tab. 2. Summary of the 12 configurations tested for the R1924A-700 PMT.

4.4.1 Discussion of the chosen method to compute the test the short gates

To illustrate the findings obtained from the methods discussed earlier, we will consider the example of HV of -900 V, a short gate of 200 ns and a delayed one of 12000 ns.

4.4.1.1 First method: graphical cuts using TCutG

For this method, we plot the PSD ratio in front of the energy measured for each event.
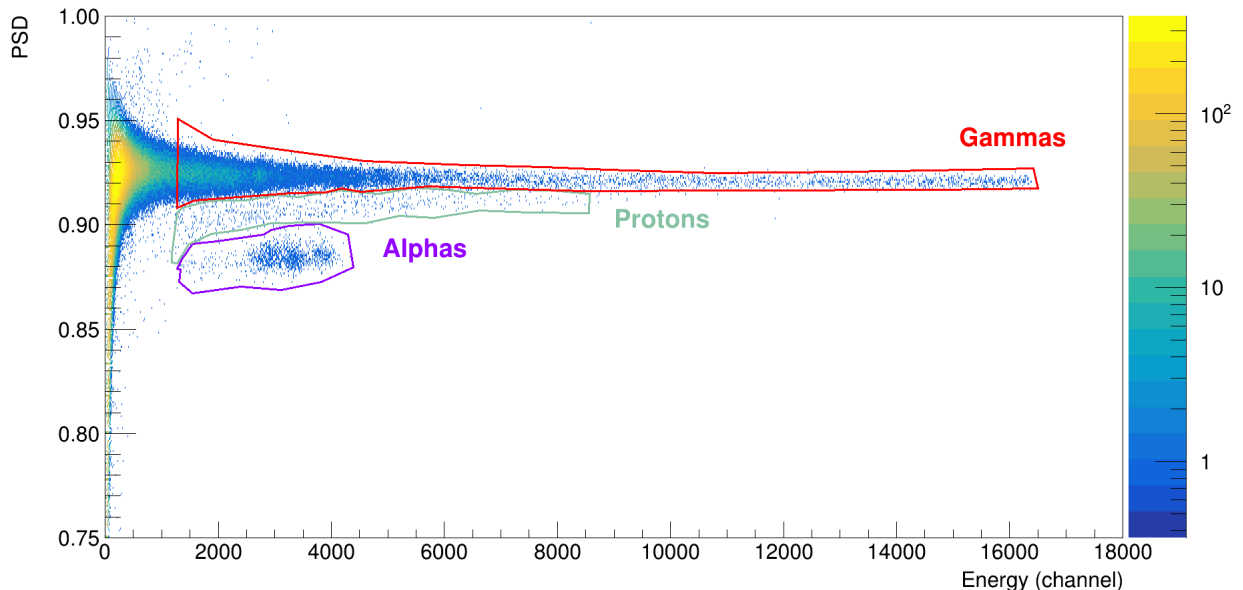

Fig. 7. PSD in front of the EnergyPSD in front of the Energy for a HV of -900 V and a short gate of 200 ns. Three graphical cuts were implemented, corresponding to the gamma, proton and alpha regions.

Using the TCutG functionality, we delimited the regions in which we know that α-particles, proton and high-energy γ-rays are, as shown in Fig. 7. The violet region represents the (n, α) reactions in the crystal, while the green region corresponds to the

(n,p) reaction, both products of the reaction of neutrons with ^{35}Cl. The high-energy gamma region is delimited in red.

To calculate the FOM value, we have depicted the projection of the the three graphical cuts delimited in Fig. 7, including and excluding the proton one. We can see that the alpha and gamma PSD value can be well distinguished visually without protons. We can observe that the delimited region for protons is closely adjacent to that of α-particles, making it challenging to distinguish them clearly in the PSD spectrum. Even though, we can fit the alpha and gamma peak with two Gaussian functions in both cases, obtaining a similar fitting values and thus, a similar FOM value.

Using the optimised parameters that adjust best the alpha and gamma peaks, we can calculate the FOM and its corresponding error. We can use the Fit Panel tool incorporated in ROOT software to fit the data.

As we can see in Fig. 8, when not including the proton graphical cut, the region between the alpha peak and the gamma one flattens, and the two peaks are perfectly discriminated using PSD. When including the three graphical cuts, a bump appears in the region between the alpha and gamma peaks, linking both curves. The proton peak is not clearly resolved, and therefore, with these parameters (HV = -900 V, short gate = 200 ns), we do not have a good α-proton or γ-proton discrimination.
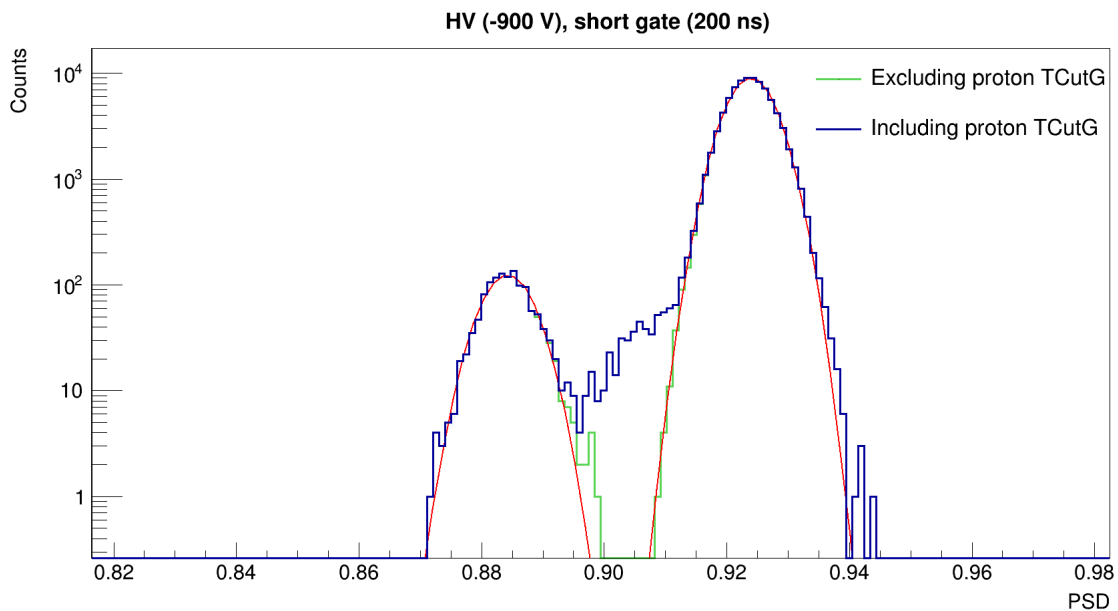

Fig. 8. Comparison between the PSD spectrum with (blue) and without (green) considering the proton region. The red line corresponds to the fitting of the alpha and gamma peaks.

Nevertheless, including or excluding the proton cut does not affect the fitting of the

gamma and alpha peaks. This leads us to consider implementing a cut at low energies only, simplifying the analysis and facilitating the determination of parameters. Since the charge integral depends upon the integration gate and the HV supply values, the positions of graphical cuts also vary for each case.

4.4.1.2   Second method: vertical cuts

To compute the FOM value, we need to repeat the previous procedure exchanging complex graphical cuts by a simple vertical cut.

As we can see in Fig. 9, there is a vertical red line in E=1000 channel. We have set this lower limit because for low-energy γ-rays, there is a higher number of counts (yellow) than in the other part of the spectrum, where high-energy γ-rays and alpha regions (green-blue). This value coincide with the start of the alpha region, delimited in violet in Fig. 7 in 4.4.1.1, First method.
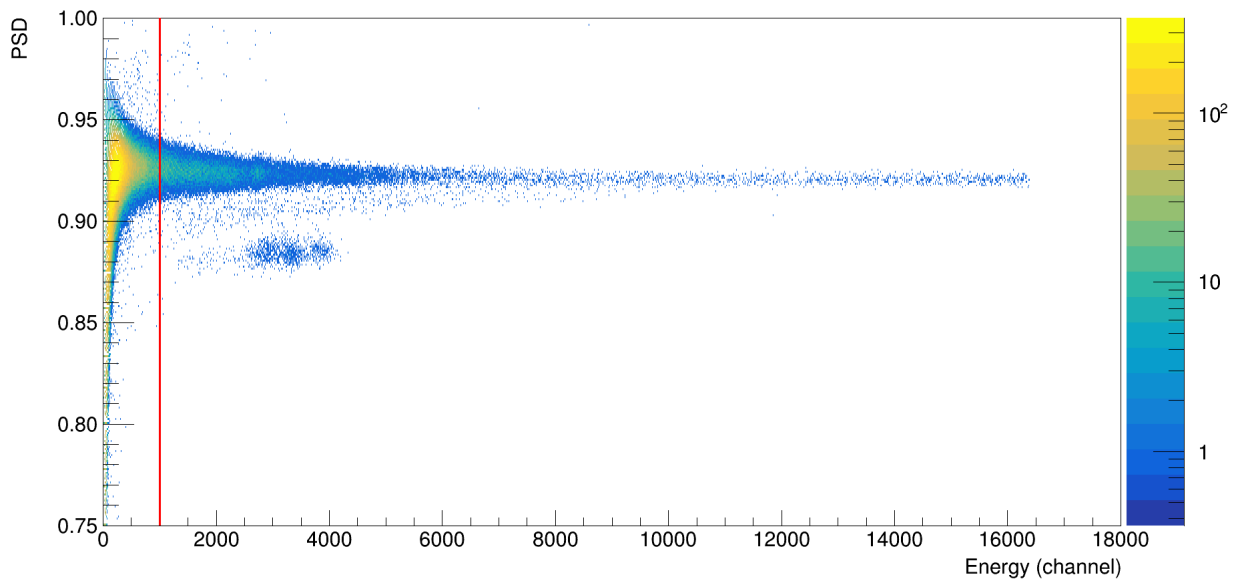

Fig. 9. PSD in front of the Energy for a HV of -900 V and a short gate of 200 ns. A vertical cut was implemented in E=1000 channel.

After applying the cut, we have to make a projection of the PSD ratio in the x-axis, representing the number of events as a function of the PSD. By doing so, we can adjust the two peaks that appear, the alpha one with a lower PSD ratio and the gamma one, with the higher value as done in Fig. 10.
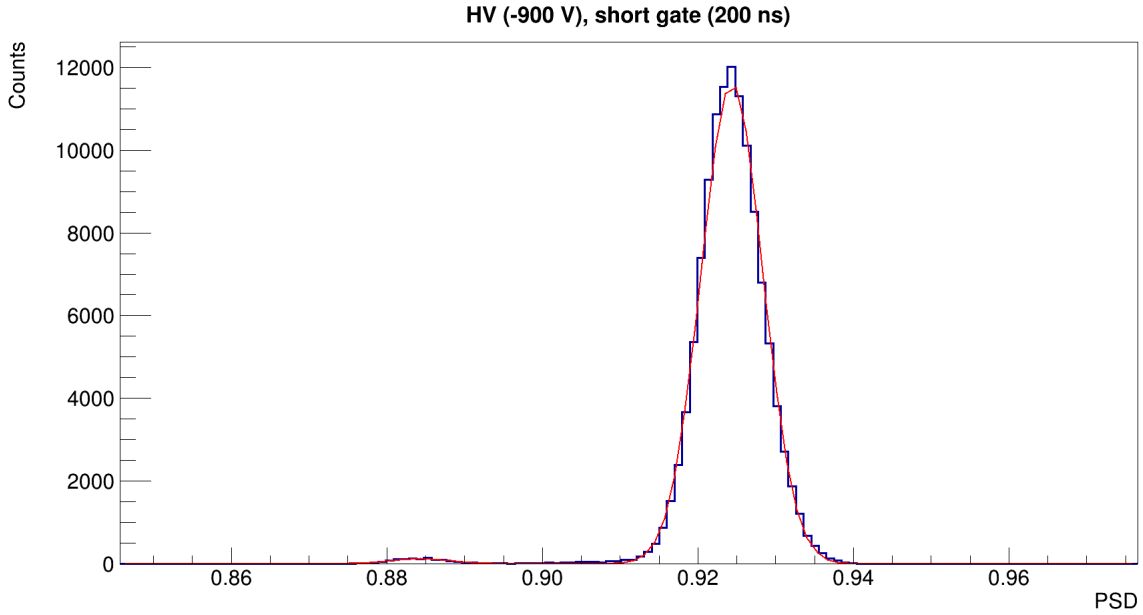
Fig. 10. PSD spectrum for a HV of -900 V and a short gate of 200 ns. We can see that there are two peaks: the small peak around 0.885 PSD, which corresponds to the α-particles and the higher one, at 0.925 PSD consisting of the γ-rays.

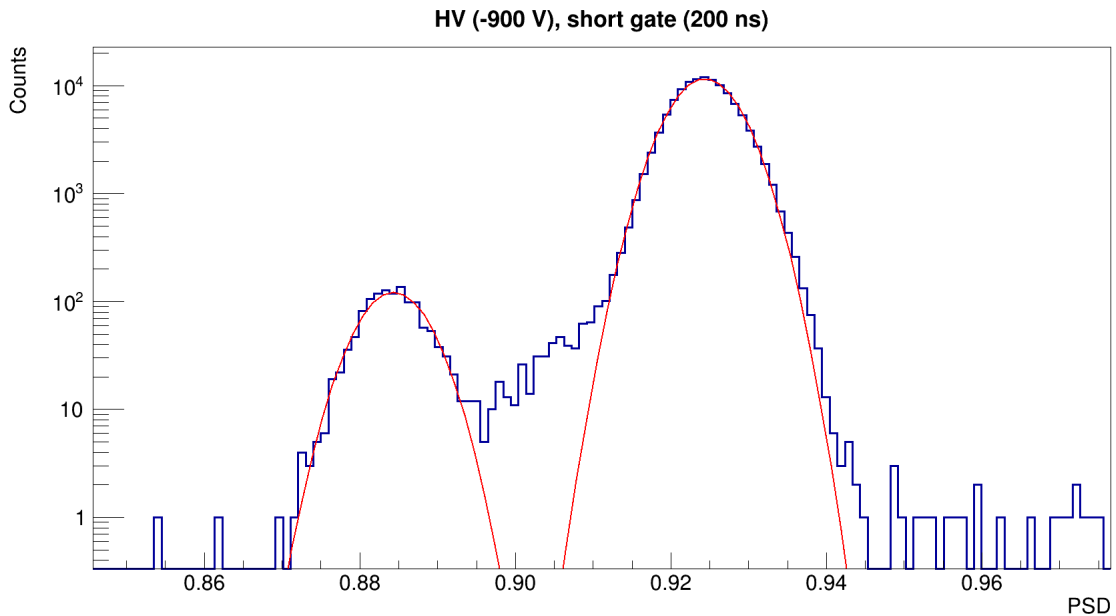For a better visualisation, we can set the y-axis to a logarithmic scale after fitting

Fig. 11. PSD spectrum for HV of -900 V and a short gate of 200 ns in logarithmic scale in the y-axis. We can see that there are two peaks: the small peak around 0.885 PSD, which corresponds to the α-particles and the higher one, at 0.925 PSD consisting of the γ-rays.

In the previous figure, Fig. 11, we can see that there is a bump between the two peaks,

which we can infer corresponds to the protons. In Fig. 9, we observe a banana-shaped region below the gamma peaks, very close, which indicates the presence of protons. It is evident in this way why there is not enough clear separation.

Once we have adjusted the two Gaussian functions to the PSD graph, we need to use the fitting parameters to compute the FOM α/γ value and its error.

Type of cut	Including the proton region	FOM α/γ
Graphical	No	2.26 ± 0.03
Graphical	Yes	2.22 ± 0.03
Vertical	Yes	2.14 ± 0.03

Tab. 3. Comparison between the FOM α/γ values obtained with graphical cuts, including and excluding protons, and with the vertical low energies cut for a high voltage of -900 V, a short gate value of 200 ns and a delayed gate of 12000 ns.

Comparing the FOMs considering those three from Tab. 3, provides a comprehensive evaluation of the discrimination strategies employed. This analysis enables us to determine that the optimum FOM value is obtained through a more refined selection of regions, with graphical cuts in the PSD vs Energy plots where particles are present. However, we have opted to analyse the various potential short gate values with the vertical cut method, due to having less uncertainty in the number of counts included in the cut region.

4.4.2 Optimal voltage and gate parameters

As we have just explained the procedure followed to obtain the FOM value step-by-step, the FOM values calculated for the 12 configurations under study are listed in the Tab. 4. The measurements have been taken in for two hours, obtaining enough statistics.

HV= -900 V		HV= -1000 V		HV= -1100 V	
SG (ns)	FOM α/γ	SG (ns)	FOM α/γ	SG (ns)	FOM α/γ
200	2.14 ± 0.03	200	2.30 ± 0.11	200	2.28 ± 0.09
300	2.15 ± 0.10	300	2.28 ± 0.10	300	2.36 ± 0.09
400	2.33 ± 0.08	400	2.55 ± 0.10	400	2.49 ± 0.11
500	2.14 ± 0.09	500	2.51 ± 0.09	500	2.26 ± 0.04
LG = 12000 ns		**LG = 14000 ns**		**LG = 16000 ns**	

Tab. 4. FOM α/γ values of the 12 configuration parameters for the R1924A-200 PMT.

From Tab. 4, we can see that the best FOM α/γ value is the one corresponding to a HV of -1000 V and a short gate of 400 ns. Since it is the best possible configuration regarding the FOM value compatible with this PMT, it would be the best choice of parameters

for a further analysis in the second CMAM experience. But another important feature must be taken into account: the possible and useful resolution of the proton peak. Using a higher voltage supply value, we can see that the FOM value corresponding to a short gate of 400 ns has a very similar value to the ones previously discussed. Moreover, it can discriminate the proton peak from the other two, as can be seen in Fig. 12.

As stated before, the more favourable scenario where we can discriminate between three types of particles (namely α-particles, γ-rays and protons) is a HV of -1100 V and a short gate of 400 ns. In this particular case, we have obtained that the FOM value for α/proton is 1.33 ± 0.14, while for γ/proton, the FOM value is 1.55 ± 0.19.

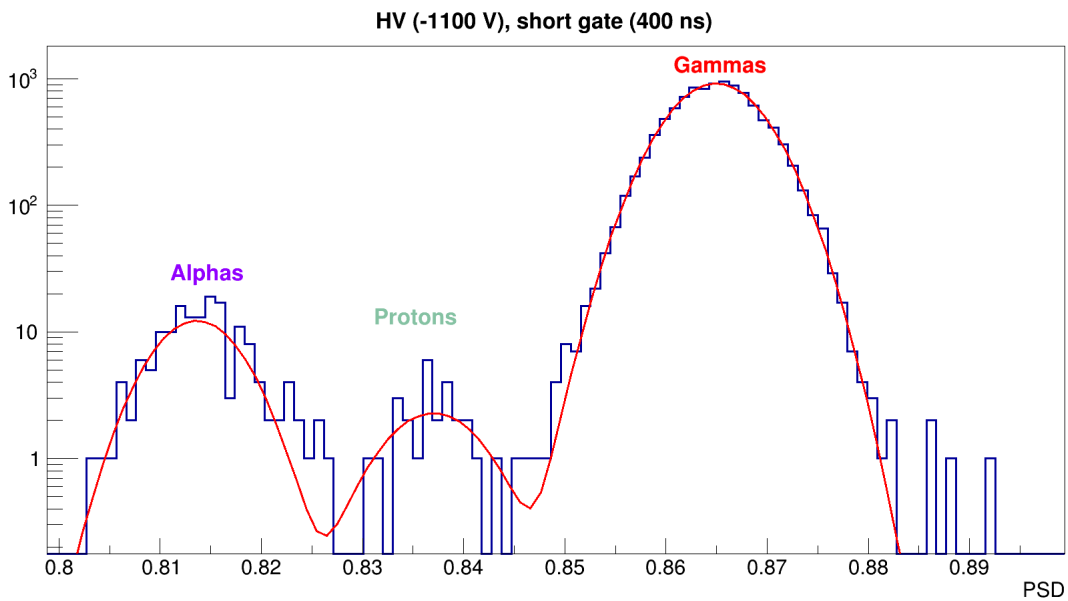**Fig. 12.** PSD spectrum for HV of -1100 V and a short gate of 400 ns in logarithmic scale in the y-axis. The fitted peaks correspond to α-particles, protons and γ-rays, respectively.

4.5 HAMAMATSU PMT: R6233-100

We aimed to compare measurements using two different PMTs while keeping the measurement conditions consistent. Due to the availability of PMTs for simultaneous experiments, we used the R6233-100 model for the initial measurements in the coaxial mode. For the ongoing measurements at CMAM, we are employing the R1924A-700 model.

The different features of each PMT are gathered in Tab. 5.

	PMT R1924A-700	PMT R6233-100
Effective area diameter (mm)	22	70
Wavelength range (nm)	(300, 500)	(300, 650)
Wavelength transmission peak (nm)	400	420
$V_{\text{cathode to anode}}$(V)	1200	1000

Tab. 5. Comparison between the most relevant parameters of the two tested PMT.

We were only able to conduct a testing with a voltage, HV of -900 V, while varying the short gates. We need enough statistics in order to properly adjust all the parameters. As a result, it is important to experiment with various time measurements before the PSD discrimination can be clearly seen. Following this, measurements were taken for 10, 20, and 30 minutes. Due to the low statistics, we extended the test duration up to an hour. Although it could be seen visually, the FOMs did not provide sensible values for some short gate values due to still having little statistics. From the two better plots which correspond to a short gate of 200 ns and 400 ns, we decided to make a 15 hours measurements in order to have the maximum possible statistics in a reasonable time and be able to calculate the FOM value.

We have gathered the results in Tab. 6.

Measurement time=15h	
HV= -900 V	
SG (ns)	**FOM α/γ**
200	2.83 ± 0.05
400	1.96 ± 0.06
LG=10000 ns	

Tab. 6. FOM α/γ values of the 2 most favourable short gates for HV of -900 V, with the R6233-100 PMT.

This study needs to be systematically completed and expanded for verification.

5 Measurements of LaCl₃ response with 10 MeV proton beam on CsI target

In the previous section we have explained how we have tested our detection system (crystal+PMT+Digitiser) in the lab with a weak[252]Cf source. In order to get enough statistics we needed to take measurements of several hours due to the low counting rate, especially for neutrons. This is why we concluded that these measurements should be taken in an environment with higher neutron fluxes such as an accelerator facility.

The facility chosen for these measurements is the CMAM external microbeam line. To perform the measurements we need a neutron beam. In this case, it is necessary to use a target that produces neutrons from protons. As depicted in the Fig. 13, we will employ a CsI target, which serves as a scintillator, enabling us to visually identify the impact point of the beam.
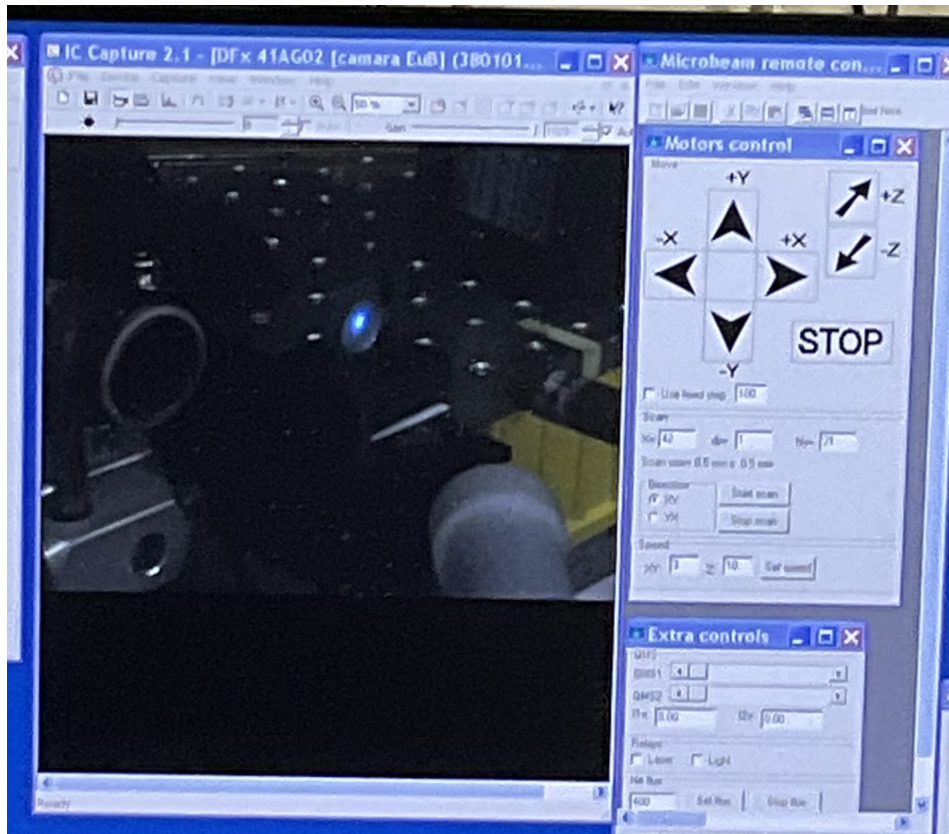
Fig. 13. This image demonstrates the scintillation characteristics exhibited by CsI when bombarded with 10 MeV protons. It also shows the "Motors control" panel to move the platform where the target is, as explained in the 5.2 section.

After using the proton beam and the same CsI target during all the measurements, the CsI target ended up getting burned due to the energy of the beam as we can see in Fig. 14.
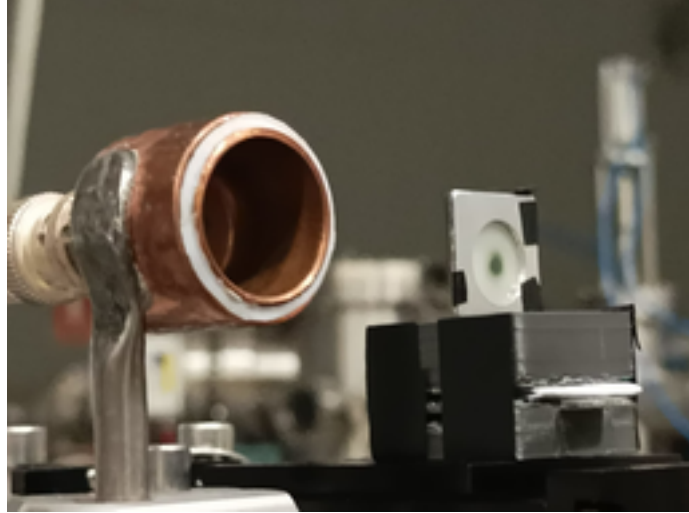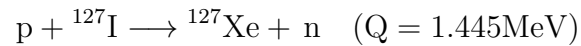
Fig. 14. This image shows the CsI target already burnt at the beam spot and the Faraday cup to measure the beam current just behind.

The proton beam will mainly interact with the ^{127}I, through the reaction:

$$p + {}^{127}I \longrightarrow {}^{127}Xe + n \quad (Q = 1.445 \text{MeV})$$

so protons with E=10 MeV can produce neutrons with energies up to 8.555 MeV, which belongs to the fast neutron range.

As explained before, the aim of the CMAM measurements is to test the LaCl$_3$ detector in coaxial configuration with the proton beam, to infer the position of the Bragg peak from the detection of γ-rays and neutrons. In our case, since the Bragg peak lies always in the same position due to the low energy of the protons, the variation of the distance between the detector and the beam will emulate a Bragg peak changing in position. By adjusting the detector-to-beam distance, we can fine-tune the position of the Bragg peak.

5.1 Simulation

Simulations are often conducted prior to experiments to gain insights into the expected outcomes and optimise experimental parameters. We have used the simulations to explore different configurations of the experimental setup as well as detector arrangements, and see their impact on the results. It also has proven useful to see if simulated results agree with the theoretical prediction, and later on, evaluate their compatibility with the experimental results.

5.1.1 Simulation framework

The objective of this simulation is to replicate the CMAM experience, which aims at the measurement of the sensitivity of our LaCl$_3$ detector to the Bragg peak position. To achieve this, we simulate the source at various distances from the detector to assess the response of the detection system to position variations. This acts as if we were moving the Bragg peak. Therefore, we will study the variation in the number of neutrons and the corresponding deposited energy.

It is practical to conduct a simulation that is as near to the actual experiment as possible in order to forecast the outcomes and optimise the configuration of the setup. In our particular experiment, we use a monoenergetic proton beam of 10 MeV at CMAM which will be used to generate neutrons from a CsI target.

To reproduce the CMAM conditions, we could simulate the proton beam reacting with the target and later analyse the generated neutrons and other products. Nevertheless, modelling the generated neutrons at an energy of 8.555 MeV, which is the incoming energy of the proton beam minus the Q-value of the reaction $^{127}\mathrm{I}\,(\mathrm{p},\mathrm{n})^{127}\mathrm{Xe}$, as we mentioned before, allows us to reduce the uncertainty in the simulation and reduce the necessary computational power and thus, the computational time. As our primary focus lies on the detection of neutrons, we can confidently proceed without concerns for that particular reaction.

Opting for a direct simulation using a neutron beam needs acknowledging the inherent limitations in accuracy. However, this approach remains valuable solely as a means to gain a general understanding of the expected outcomes at CMAM, rather than providing precise results.

As we said before, our scintillator has a truncated conical shape of 16 mm of height, the largest diameter being 22.5 mm and the smallest, 16 mm, coated with a 2 mm thick layer of PTFE and 0.1 mm of Aluminium shielding. To detect the incident particles, we have incorporated a flux detector for counting purposes, as we can see in Fig. 15.
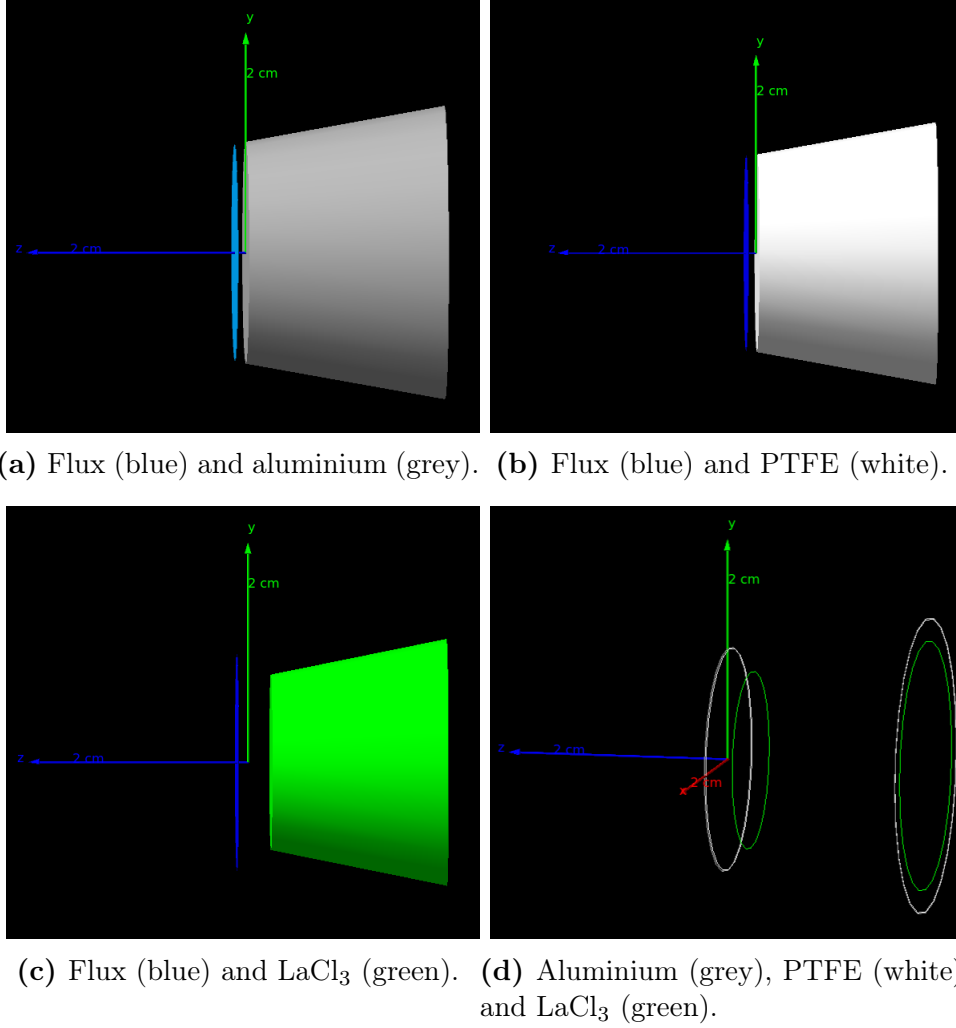
(a) Flux (blue) and aluminium (grey). **(b)** Flux (blue) and PTFE (white).

(c) Flux (blue) and LaCl₃ (green). **(d)** Aluminium (grey), PTFE (white) and LaCl₃ (green).

Fig. 15. **(a),(b),(c)** Visualisation of the LaCl₃ scintillator layers in the yz plane. A flux detector has been incorporated to measure the number of counts that arrive to the detector. **(d)** Wire-frame 3D representation of LaCl₃ spatial distribution without coatings.

Since we are interested in the deposited energy, we do not simulate the scintillating response of the LaCl₃ crystal that enters the PMT. If we were to include this complete interaction in the simulation, it would require the incorporation of the quartz window. However, since our main focus is on simulating neutrons, this omission does not affect our intended outcomes.

The neutrons, when impacting on LaCl₃ , produce essentially two processes with a significant cross section. We can know the contribution of each reaction channel by separating their contributions from the total: the α-channel, $^{35}\mathrm{Cl}(n,\alpha)^{32}\mathrm{P}$, and the p-channel, $^{35}\mathrm{Cl}(n,p)^{35}\mathrm{S}$.
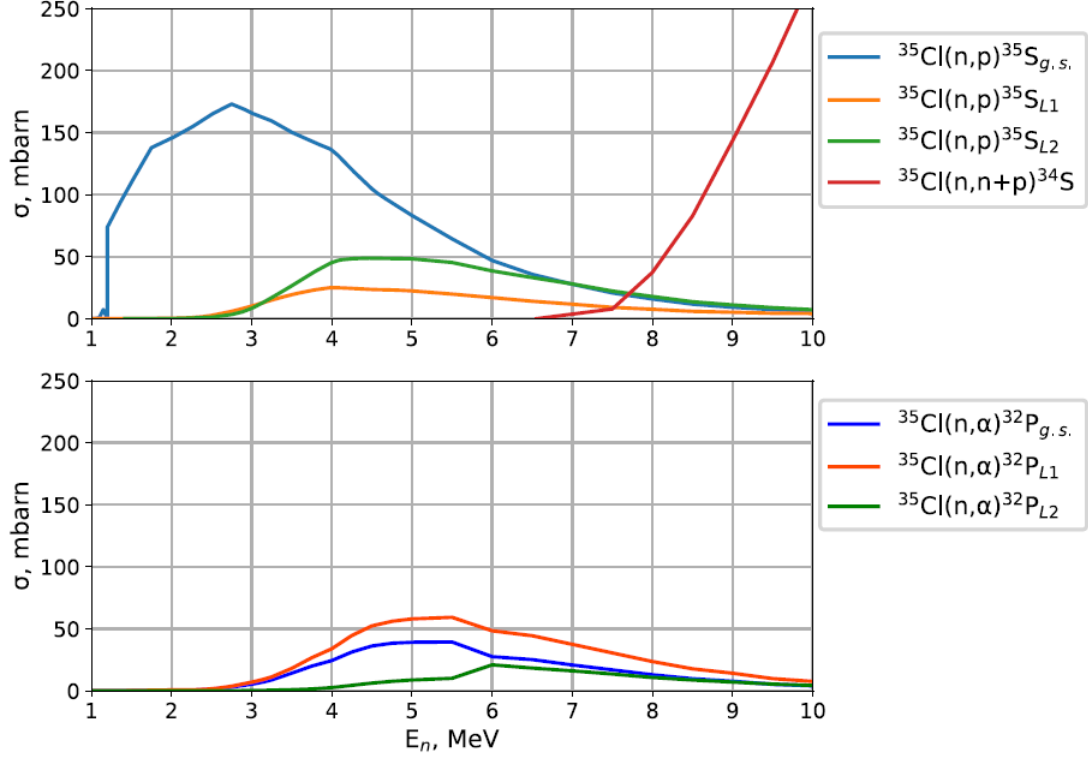
Fig. 16. ^{35}Cl(n,p)^{35}S cross section including ^{35}Cl(n,n+p)^{34}S (top) and ^{35}Cl(n,α)^{32}P cross section (bottom) including the first three energy levels: ground state (g.s.), first excited state (L$_1$) and second excited state (L$_2$). Image taken from [8].

At the same time, the ^{35}S and ^{32}P products in excited states emit gamma rays which are also detected. As we can see in Fig. 16, the states of the ^{35}S and ^{32}P with a significant cross section are the ground state (g.s.), the first excited state (L$_1$) and the second excited state (L$_2$). From NuDat [11], we have obtained that the energy levels of the three states of each residual nuclei form the ground state as the zero-energy reference. For ^{35}S, $E_{L_1} = 1572.378$ keV and $E_{L_2} = 1991.28$ keV, and for ^{32}P, $E_{L_1} = 78.06$ keV and $E_{L_2} = 512.70$ keV. Therefore, since the excited states will end up decaying, γ-rays with the energy level values will be detected. In addition, by plotting that of α-particles and protons, we have all four contributions to analyse.

5.1.2 Simulation results

The simulation has been done with Geant4 simulation packages [10]. We want to study the total energy deposition as well as each contribution from the products of the reactions with ^{35}Cl isotope present in the LaCl$_3$ scintillator: α-particles, protons, ^{32}P and ^{35}S. We have also obtained the energy distribution of the neutron source and the hit positions in the x, y and z directions of the total and of each contribution.
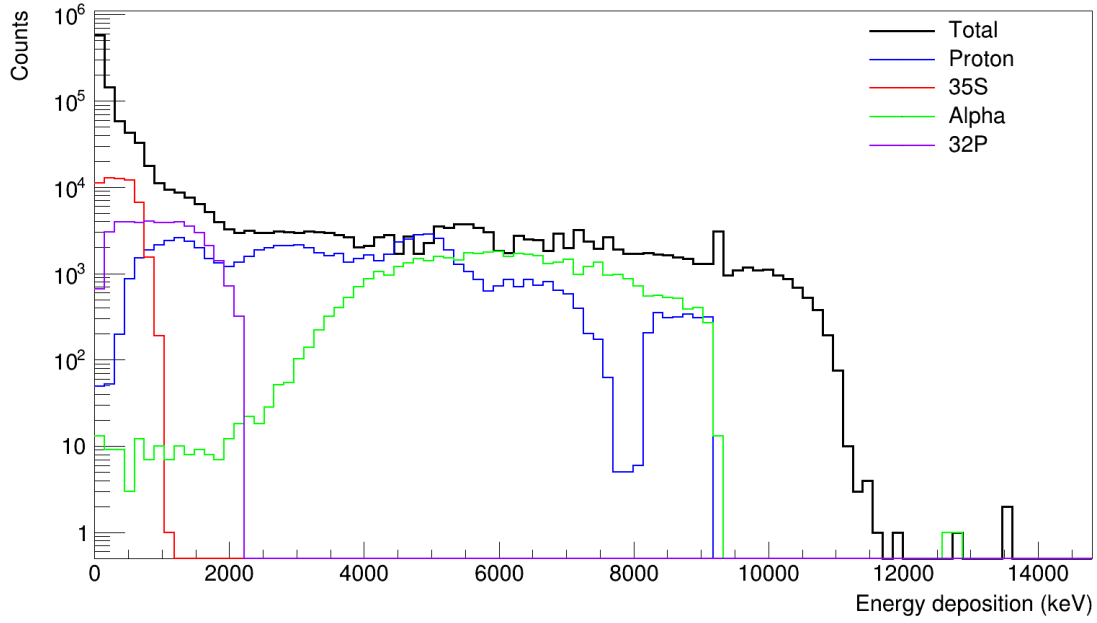
Fig. 17. Total energy deposition and its four main contributions: proton and ^{35}S contributions from the ^{35}Cl$(n,p)^{35}$S nuclear reaction, and α-particle and ^{32}P form the ^{35}Cl$(n,\alpha)^{32}$P reaction.

In order to examine the results, we will investigate several target distances. Specifically, positions of 160 mm, 170 mm, and 180 mm.

One of the key findings of interest is the total deposited energy and its individual contributions. As becomes evident from Fig. 17, the proton and α-particle contributions exhibit a broader energy distribution that spans entirely the shown energy spectrum than ^{35}S and ^{32}P. This disparity arises from the energy and momentum conservation. The residual nuclei have a greater mass compared to the protons or α-particles, resulting in less kinetic energy during the reaction and in consequence, their energy deposition is lower.
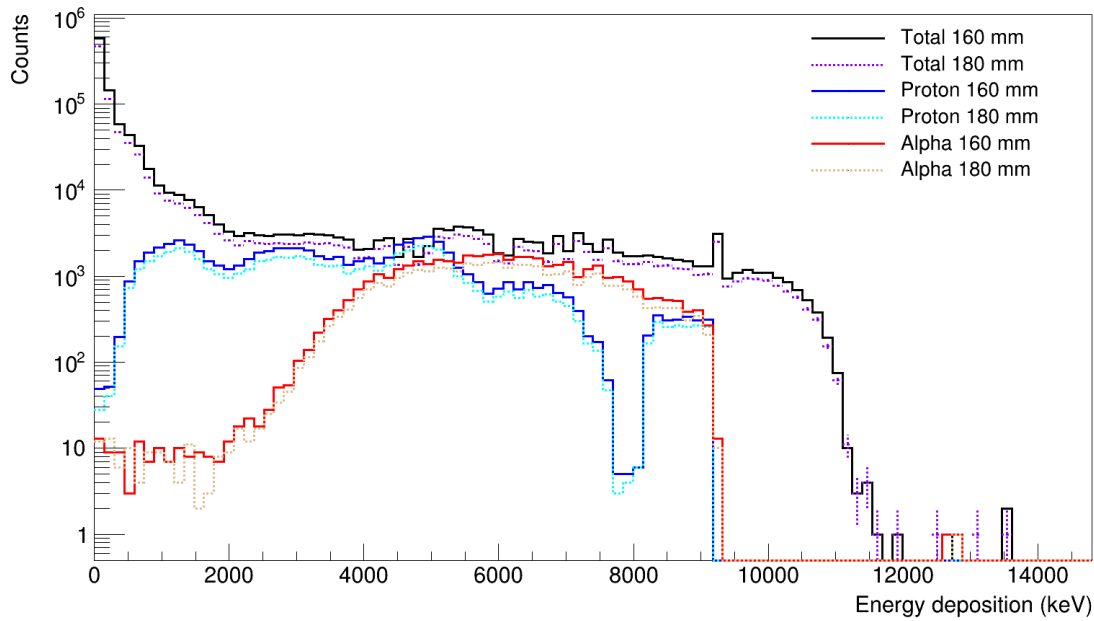
(a) Total number of events within the energy deposition range with proton and α-particles contributions.
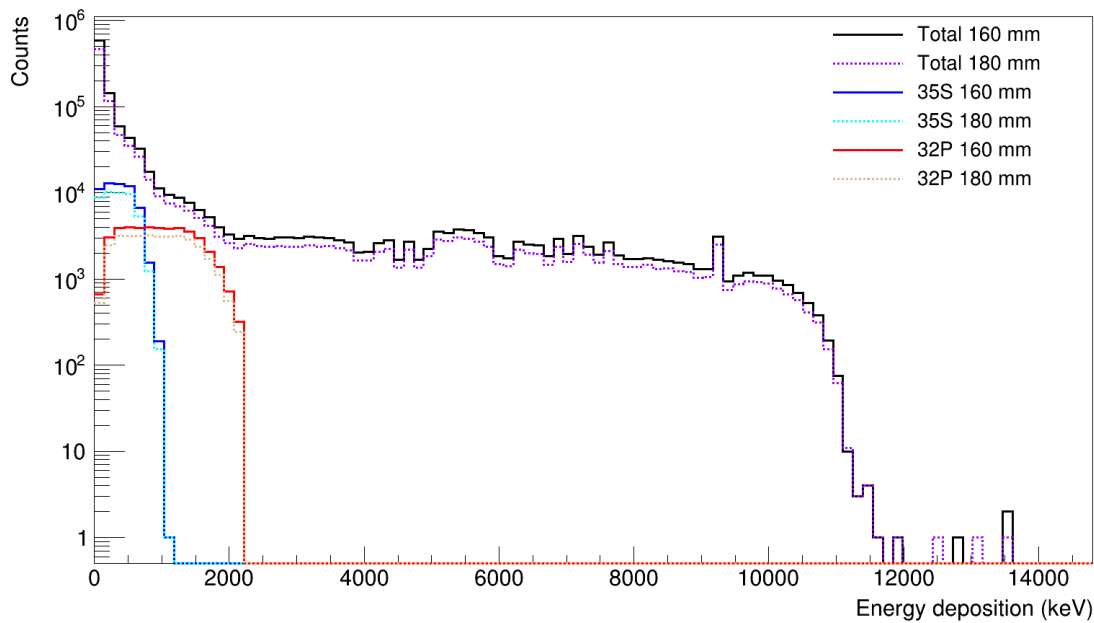

(b) Total number of events within the energy deposition range with ^{35}S and ^{32}P contributions.

Fig. 18. Comparison of the total deposited energy with its main contributions for the beam-detector distances of 160 mm and 180 mm. In **(a)**, including light particles and in **(b)**, the residual nuclei. The solid lines in both graphs correspond to a distance of 160 mm, while the dashed lines represent a distance of 180 mm. This comparison allows for an analysis of the different particle contributions at these extreme distances.

As depicted in Fig. 18, increasing the distance between the detector and the beam results

in a decrease in the total number of counts. This is primarily due to the solid angle effect: the closer the source and the detector are, the greater the solid angle and, consequently, the higher number of detected particles. The profiles of the various curves remain largely similar, though with a lower count rate.
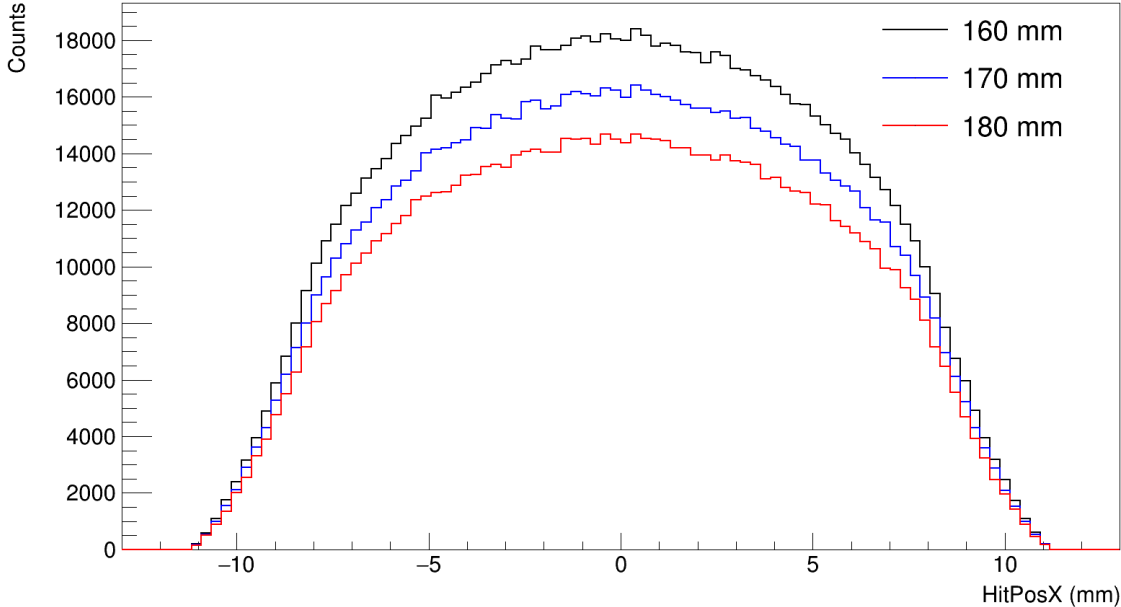
(a) Hits detected in x direction.
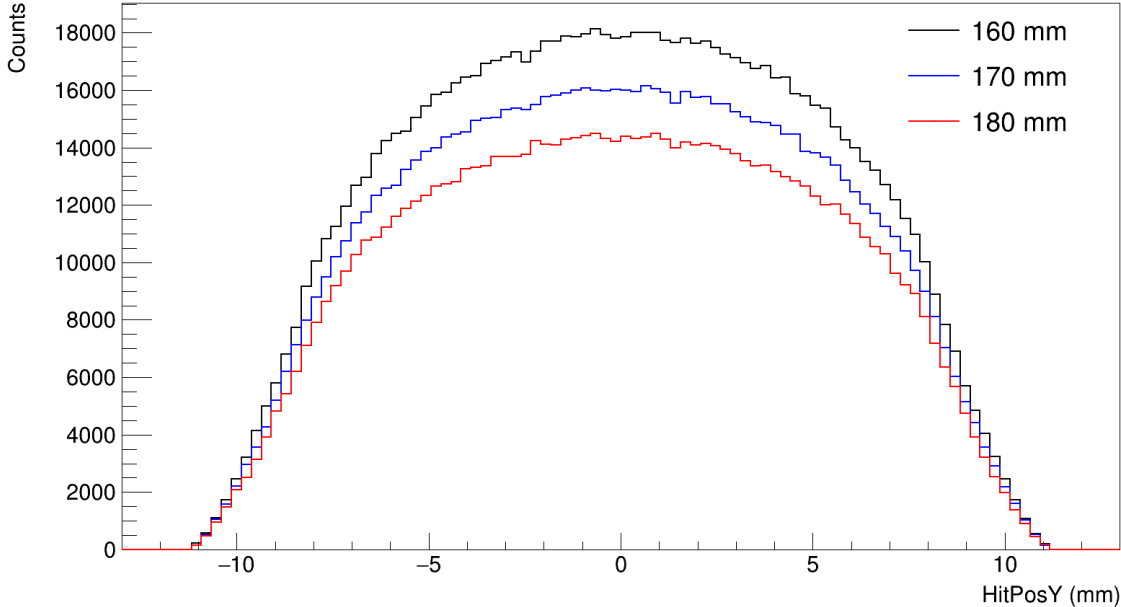
(b) Hits detected in y direction.

Fig. 19. Hits detected in the x and y direction for three source-detector distances: 160 mm, 170 mm and 180 mm.
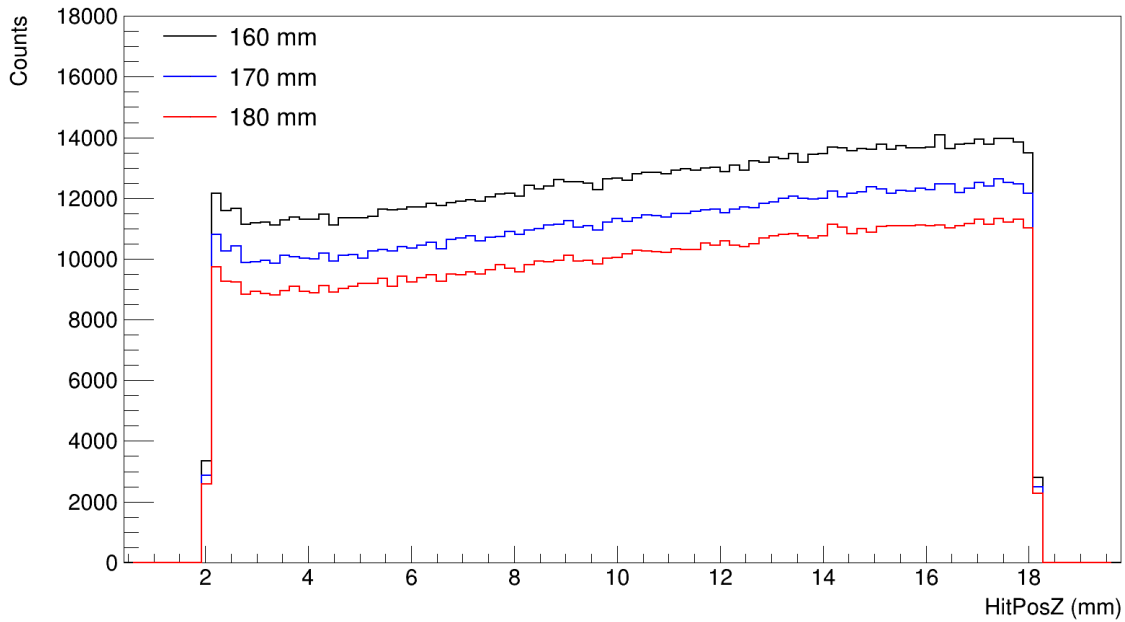
Fig. 20. Hits detected in the z direction for three source-detector distances: 160 mm, 170 mm and 180 mm.

Based on Fig. 19, it is evident that the number of hits in the x and y directions exhibit symmetry. It is important to note that the z-axis aligns with the beam direction, as depicted in Fig. 15. When the solid angle of the detectors decreases, indicating an increased distance between the beam and the detector, the number of hits along both the x and y directions decreases, as expected.

We have also plotted the hits in the z-direction, Fig. 20, revealing that the majority of hits occur towards the rear side of the crystal, where the diameter is bigger. This is primarily because the larger diameter provides a greater surface area for detection, resulting in a higher number of hits. The same effect caused by the solid angle, which was previously explained, also applies to the variation in distance.

To provide a concise overview, we have represented plots illustrating the number of detected events as a function of distance. These plots allow us to observe the overall trend for each of the products' contribution.

In Fig. 21, we can see that the number of events detected in the $LaCl_3$ detector decrease when increasing the distance between the detector and the beam. This is essentially due to the solid angle effect. Consequently, a lower number of counts is detected by the detector, which is in line with our expectations.
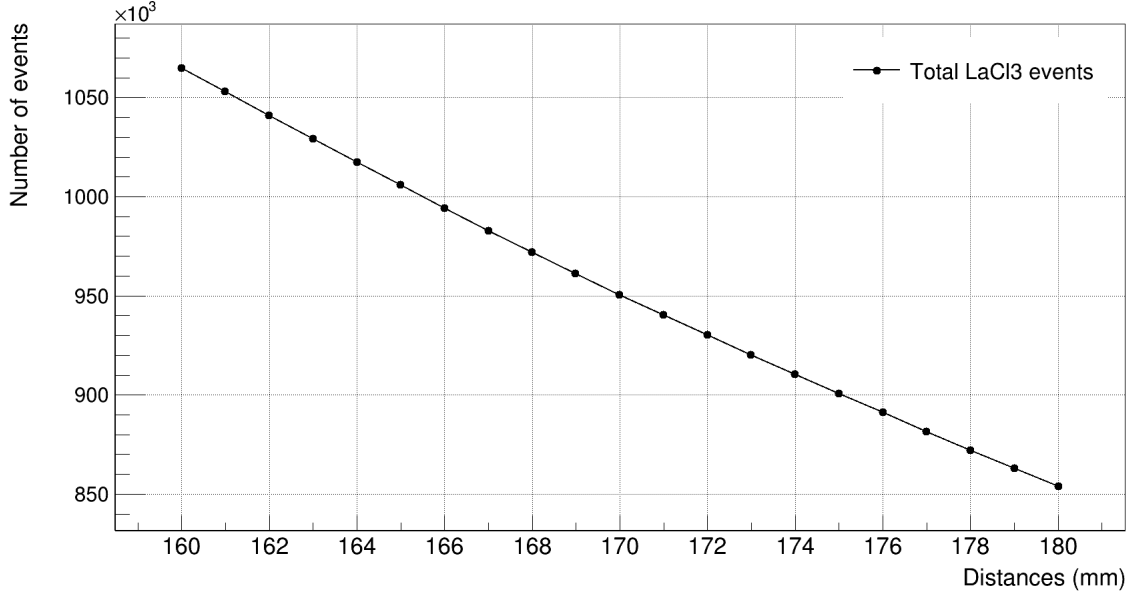
(a) Total LaCl₃ events as a function of the distance source-detector.
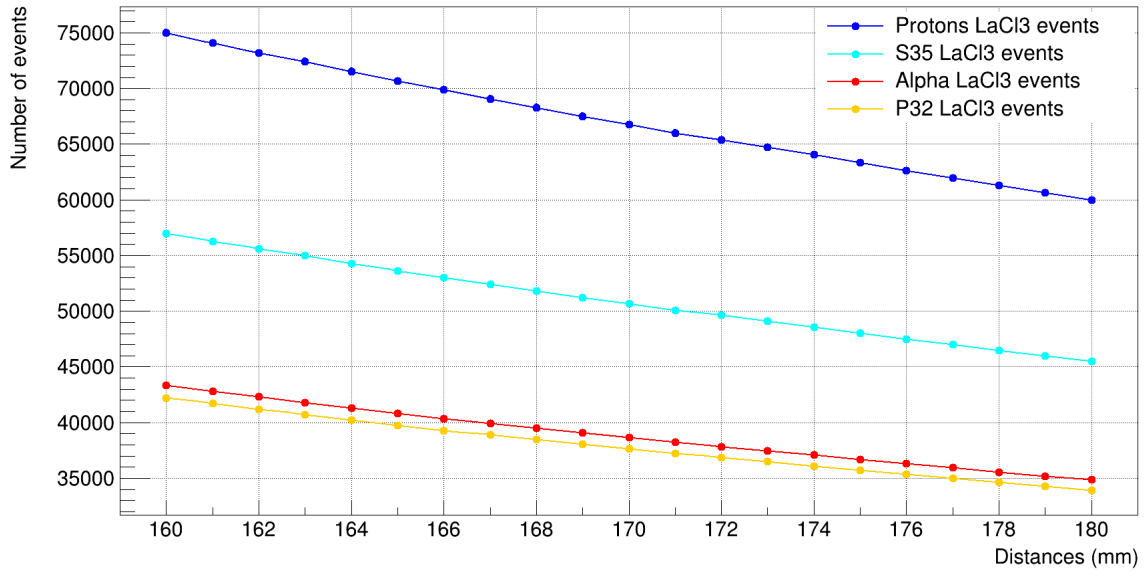
(b) Main contributions to total LaCl₃ events as a function of the distance source-detector.

Fig. 21. The top graph, **(a)**, displays the total number of events within our distance range, while the bottom graph, **(b)**, illustrates the main individual contributions. We have separated them into two graphs because the number of events differs significantly. Although all data points include y-error bars, they are negligible in size.

In Fig. 21b, we can see that the products of the two reactions,^{35}Cl(n,p)^{35}S and ^{35}Cl(n,α)^{32}P. It is evident that the primary contributors to the number of events are protons, followed by ^{35}S, both originating from the same reaction. The observed phenomenon can be attributed to the disparity in cross sections and energy threshold at which reaction channels open, as illustrated in Fig. 16. The ^{35}Cl(n,p)^{35}S reaction has a higher cross section and a

lower energy threshold at which the channel opens, for neutron incoming energy around 1 MeV. In contrast, the ^{35}Cl(n,α)^{32}P reaction opens for neutrons with incoming energy around 3 MeV. These two factors are the ones contributing to this phenomenon. This means that this particular reaction exhibits a higher number of events and, consequently, a greater probability. When comparing the other two products, α and ^{32}P, their contributions appear to be quite similar.

5.1.3 Simulation results adding a neutron moderator

Additionally, we conducted a simulation using a 5 cm thick (z-direction) polyethylene block of 8 cm in height (y-direction) and 6 cm in width (x-direction) to observe its impact on the neutron counting rate at three varying distances, as we can see in Fig. 22.

Neutrons undergo thermalisation through elastic collisions with hydrogen atoms in polyethylene, resulting in the production of thermal neutrons. Upon reaching our detector with reduced energy, we anticipate a decrease in the number of counts in the α-channel due to the Q-value of the (n,α) reaction in LaCl$_3$. Additionally, the proton channel is also diminished. This opens the possibility to use polyethylene around our crystal to thermalise and therefore reduce the contribution of neutrons coming from other sources than the beam. We need to consider that the LaCl$_3$ scintillator is sensitive to fast neutrons. In proton therapy facilities, the scattered neutrons in the walls often contribute significantly to the background. To mitigate this, we can reduce the background in our setup by shielding the detector with polyethylene.
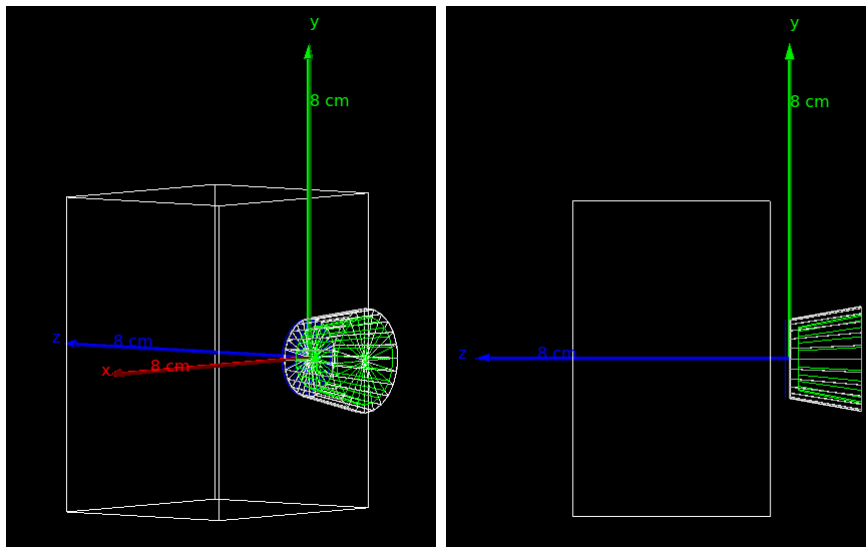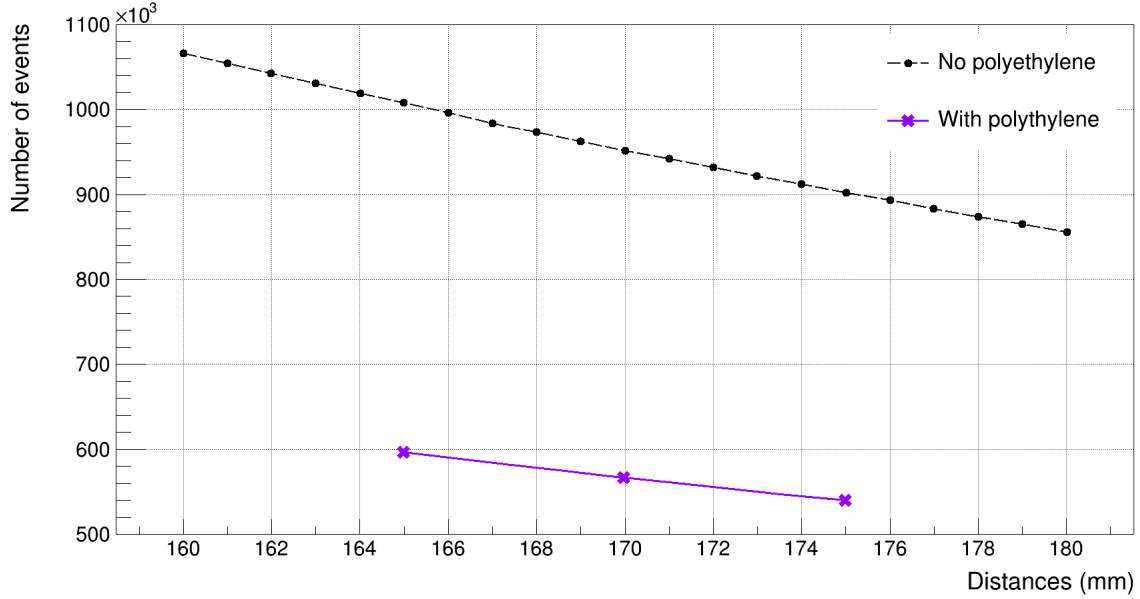

Fig. 22. A block of polyethylene with a thickness of 5 cm is shown as part of the detector setup in this illustration. Because we have not depicted the PMT device, the block appears to be large in comparison to the scintillating crystal. We can see in the right picture that the separation between the scintillator and the polyethylene block is 1 cm.

(a) Total number of events for each distance with and without polyethylene.
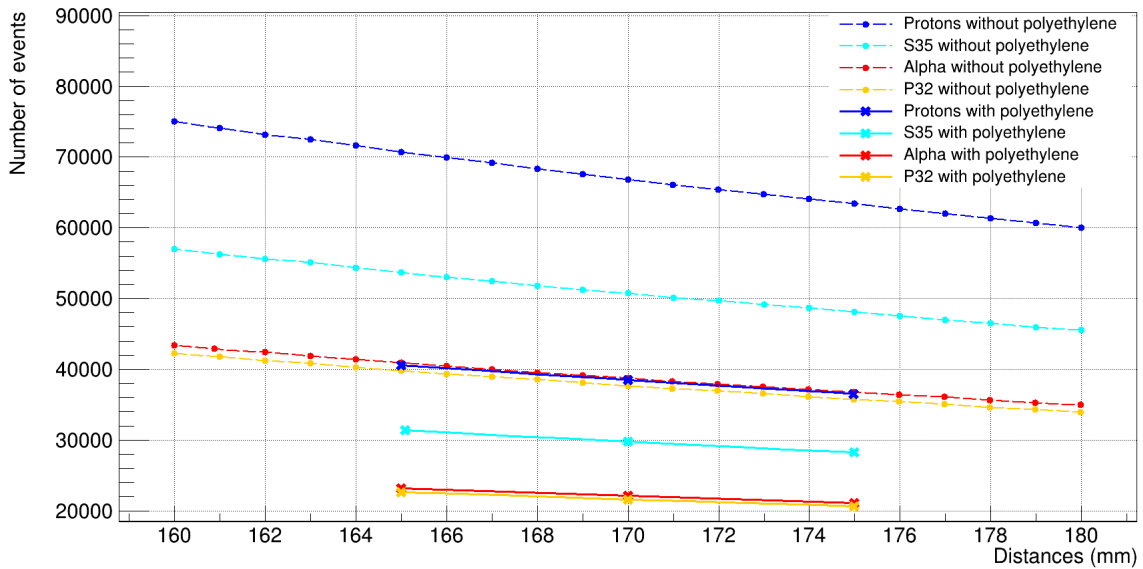
(b) Main contributions of the total number of events in the polyethylene case.

Fig. 23. The top graph, **(a)**, displays the total number of events within our distance range with and without polyethylene, while the bottom graph, **(b)** illustrates their individual contributions for measures with (solid lines) and without (dashed lines) a block of polyethylene. We have separated them into two graphs because the number of events differs significantly. Although all data points include y-error bars, they are almost negligible in size.

We have simulated the distances studied with polyethylene in the CMAM facility: 165 mm, 170 mm and 175 mm. As we can see in Fig. 23, the global trend of the plots of the total number of events and its contributions for each explored distance is exactly the

same with and without polyethylene. We can see that the number of events registered is higher in the non-polyethylene case than the one with polyethylene.
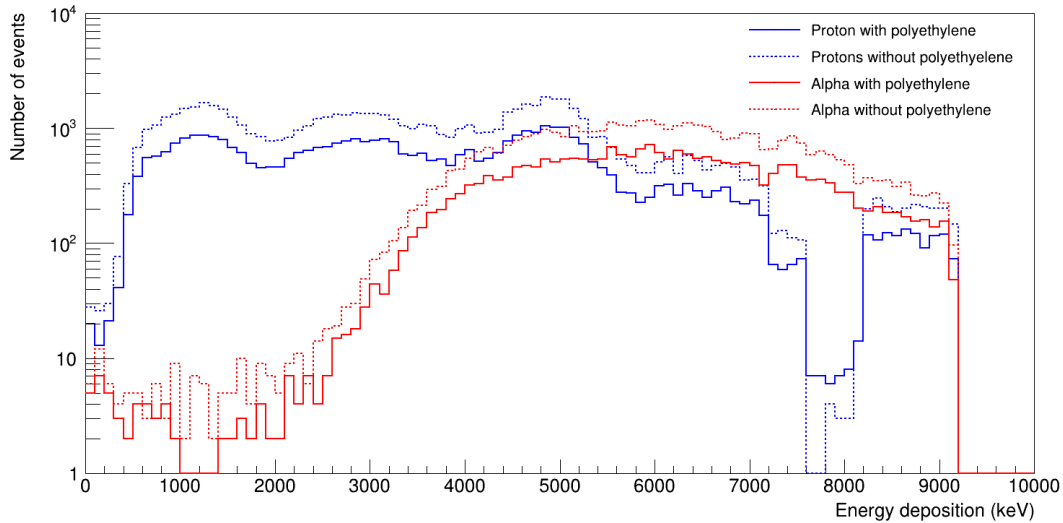

Fig. 24. Deposited energy contributions of protons and α-particles at a source-detector distance of 165 mm with and without polyethylene. To be understood as an example for all simulated distance values.

Regarding the energy deposition, we can see in Fig. 24 that the number of events for each energy deposition is lower when using a polyethylene block for protons and α-particles. This is due to the fact that these particles are the products of the neutron reactions (n,p) and (n,α). When neutrons are moderated, less neutrons interact with the ^{35}Cl present in the LaCl$_3$ scintillator, and thus the number of products of this reactions are less.

We have also computed the difference in the number of counts of the polyethylene and the non-polyethylene cases for three distances, as shown in Tab. 7. More specifically, we have computed the total and each of the four main contributions, obtaining a substantial difference in the proton contribution.

Distances (mm)	LaCl$_3$	Proton	^{35}S	Alpha	^{32}P
165	409926	30081	22294	17721	17219
170	384124	28292	20927	16613	16133
175	361224	26830	19796	15634	15170

Tab. 7. Difference in event detection between the polyethylene and non-polyethylene scenarios. The variations in the number of counts and the main contributions have been documented. These observations were made at three distinct distances separating the detector from the beam.

5.2 Proton beam results

The setup consists of a millimetre-precise platform that holds the CsI target, and allows an automated and controlled movement of its position with respect to the proton beam exit and the detector position. In Fig. 25, we can see a picture of the experimental setup in CMAM. Simultaneous measurements were conducted with other detectors to optimise beam time utilisation.
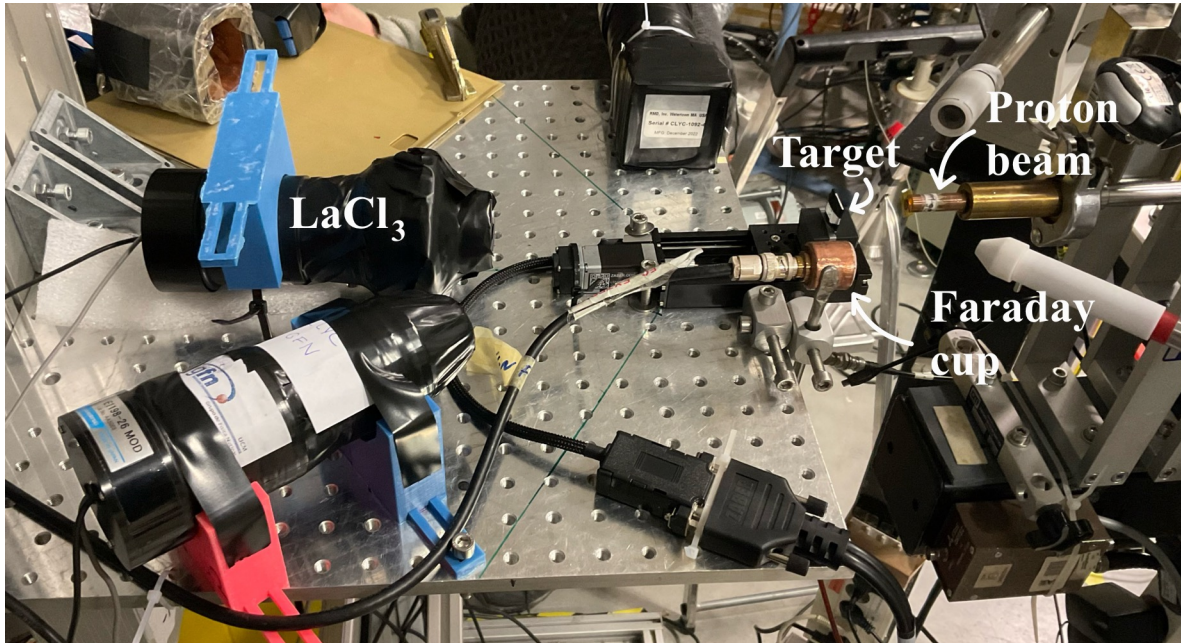

Fig. 25. A photograph capturing the experimental setup was taken during the simultaneous measurements conducted with other detectors.

We have designed a sketch, depicted in Fig. 26, to clarify the movement of the operational motor that controls the motion of the target, allowing us to observe the initial "home" configuration and the maximum allowed distance. We can see that the range of movement is 50 mm, but we will restrict the distance between the detector and the target to the 160 mm to 180 mm range.

We have created two separate sets of positions: even positions and odd ones, in stages of 2 mm in order to measurement for the entire position range in steps of 1 mm.

It is important to measurement the intensity of the beam inside and outside the vacuum chamber. For that purpose, we have used two conductive cups called Faraday cups, to collect charged particles. The amount of ions or electrons that strike the cup can be estimated from the produced current by measuring it. Unfortunately this could only be done in between measurements (runs of beam on target), but not during the measurements themselves. Furthermore, each time we had to move the Faraday cups in and out and this implies imprecision in the positioning and therefore the current measurements, as we
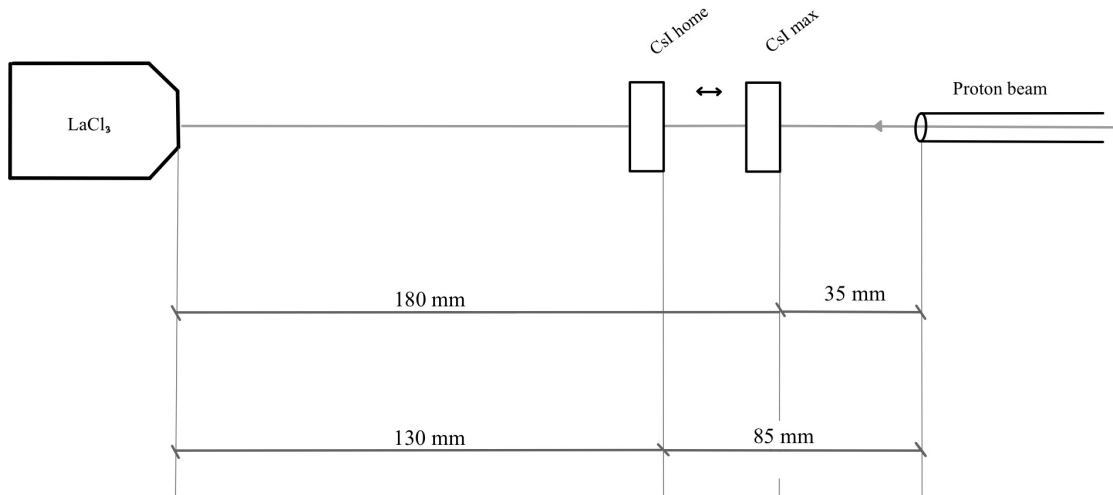
Fig. 26. CMAM setup diagram.

will see later.

5.2.1 PSD discrimination in measurements of 5 minutes
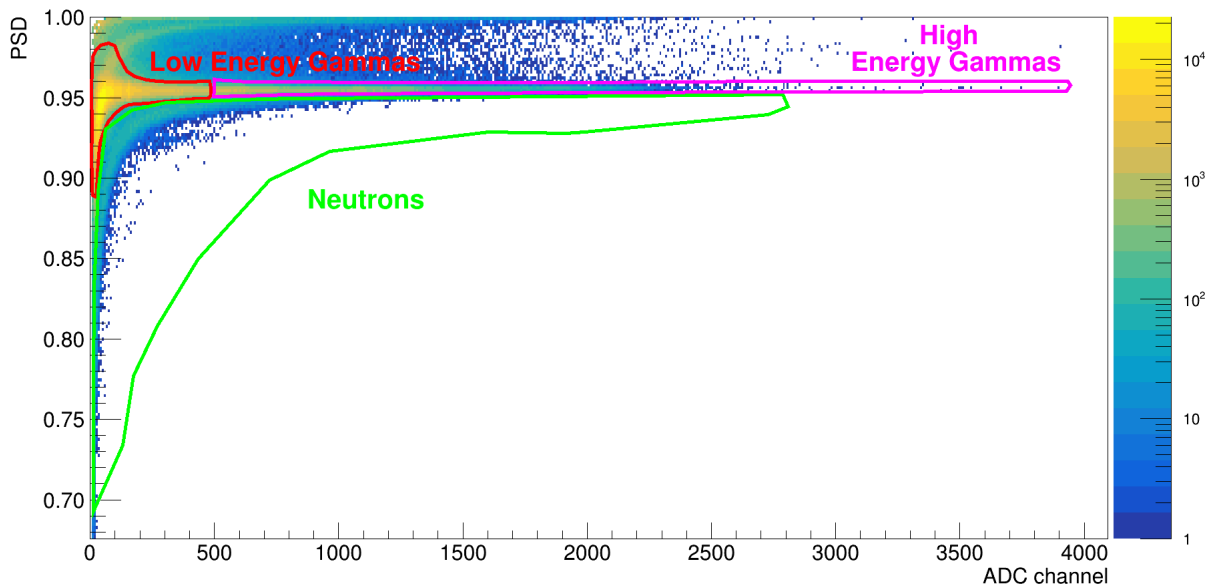

Fig. 27. PSD as a function of the ADC channel with the graphical cuts drawn for a beam-detector distance of 161 mm.

To test the detector's sensitivity to changes in the Bragg peak position, we conducted two sets of measurements. Firstly, we measured the set of even positions, ranging from 180 mm to 160 mm in increments of 2 mm. Subsequently, we repeated the measurements backwards for the set of odd positions, ranging from 179 mm to 161 mm.

Taking Fig. 27 as an example, we have included a plot of the PSD versus the ADC channel at a distance of 161 mm. The graph illustrates the different regions of interest, which have been delineated with the TCutG tool in ROOT software to carry out the further analysis.

We also conducted a background measurement at the last measured odd position, 161 mm, for a duration of 26 minutes, as shown in Fig. 28. By comparing the background plot in Fig. 28 with the beam on plot in Fig. 27, both taken at the same distance, we can observe that the high-energy gamma region and the neutron region exhibit significantly lower counts in the background scenario, which was expected.

Type of measurement	High-energy gammas	Low-energy gammas	Neutrons
Beam On at 161 mm	152568 ± 391	1775185 ± 1378	44940 ± 212
Background at 161 mm	111 ± 11	62399 ± 250	13 ± 2

Tab. 8. Number of counts of the high-energy gamma region, the low-energy gamma region and the neutron region for the background and the beam on measurements at 161 mm. The number of counts of the background have been normalised to 5 minutes, the beam on measurements' time.
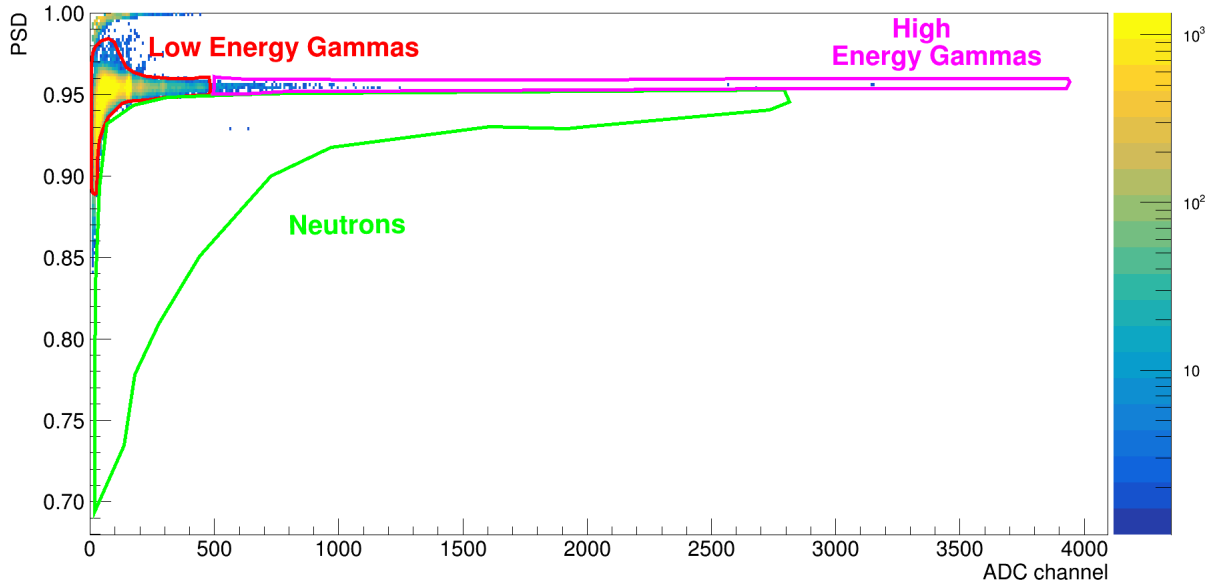

Fig. 28. Background acquired in a distance of 161 mm for 26 minutes.

As we examine the low-energy gamma region, we wanted to compare the integrals of this region between the background and beam on measurements to determine if the majority of counts in the low-energy gammas region are present in the background. According

to Tab. 8, the low-energy gamma region accounts for only 3.5% of the counts from the background measurement.

We have gathered all the results of the twenty measurements acquired from 160 mm to 180 mm in target-beam distance in Tab. 9. The second column is the beam intensity at the end of each measurement, and the integral of the three main graphical regions of interest are shown in the last three columns: high-energy gammas, low-energy gammas and neutrons.

Position (mm)	Intensity (nA)	High-energy gammas	Low-energy gammas	Neutrons
160	4.70	26503 ± 75	360520 ± 138	7686 ± 40
161	6.09	25052 ± 64	291492 ± 226	7368 ± 35
162	5.13	23568 ± 68	324156 ± 264	6589 ± 36
163	6.06	24668 ± 64	294468 ± 228	7039 ± 34
164	5.11	24066 ± 69	330922 ± 264	6870 ± 37
165	6.07	24755 ± 64	286070 ± 225	6917 ± 34
166	5.10	23237 ± 73	321246 ± 283	6848 ± 37
167	6.00	24274 ± 64	285672 ± 226	7254 ± 35
168	5.00	23941 ± 66	325747 ± 265	6874 ± 37
169	5.90	25040 ± 65	280646 ± 226	7214 ± 35
170	5.90	25183 ± 66	273349 ± 223	7370 ± 35
171	5.90	24950 ± 65	276069 ± 224	7462 ± 36
172	5.20	22741 ± 66	309721 ± 253	6468 ± 35
173	5.90	24874 ± 65	271544 ± 223	7131 ± 35
174	5.26	21978 ± 65	300455 ± 248	6114 ± 34
175	5.90	24233 ± 64	263740 ± 220	7049 ± 35
176	5.15	20530 ± 63	284581 ± 245	5527 ± 33
177	5.90	23185 ± 63	259034 ± 218	7063 ± 35
178	4.20	20932 ± 71	293049 ± 277	5670 ± 37
179	5.80	17963 ± 63	211551 ± 216	6576 ± 34
180	5.00	20224 ± 64	273815 ± 244	5780 ± 34

Tab. 9. Number of counts, normalised with the intensity, of the high-energy gamma region, the low-energy gamma region and the neutron region for each of the 20 positions explored. The intensity values have also been included for a further analysis.
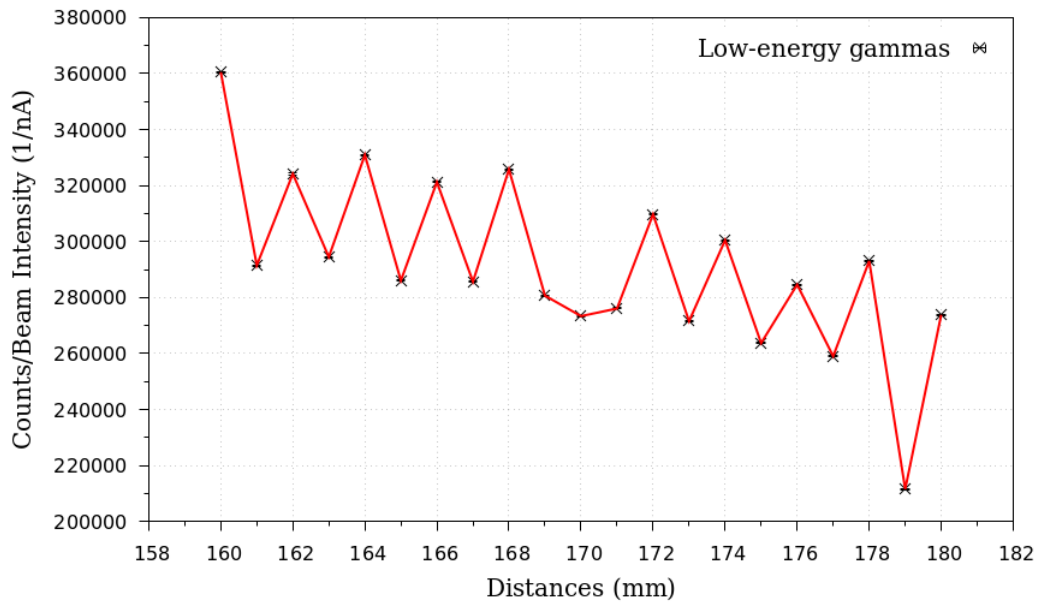
Fig. 30. Counts normalised with intensity due to intensity fluctuations as a function of the distance target-detector for the low-energy gamma region. This region is represented for 161 mm case in Fig. 27.
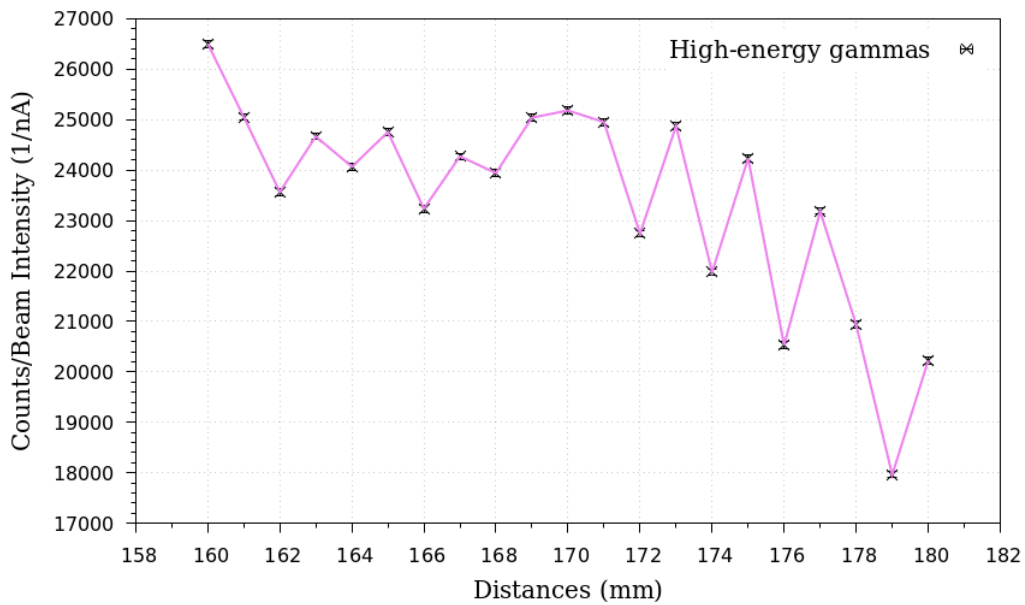

Fig. 29. Counts normalised with intensity due to intensity fluctuations as a function of the distance target-detector for the high-energy gamma region. This region is represented for 161 mm case in Fig. 27.
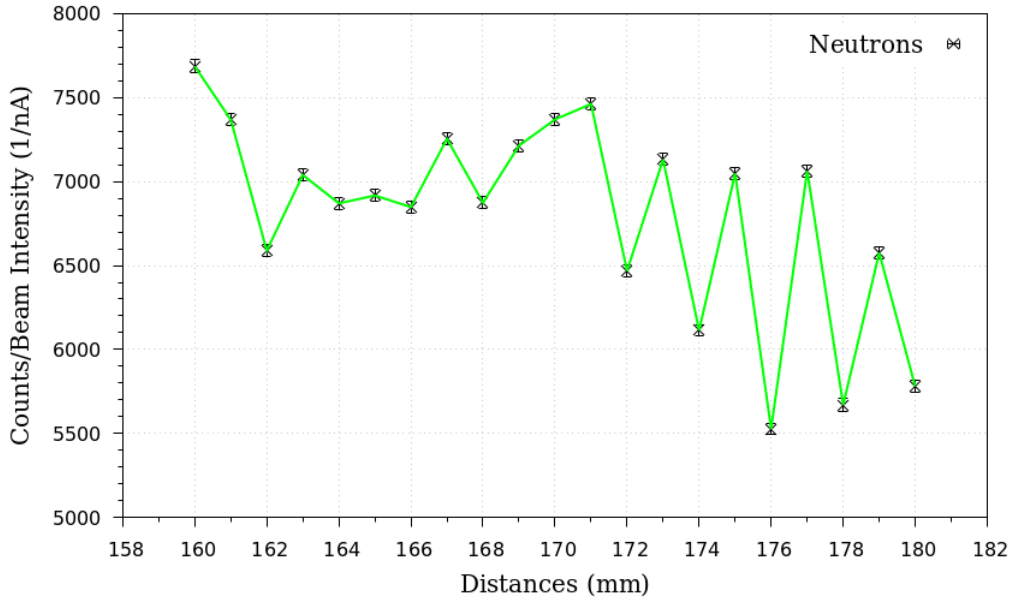
Fig. 31. Counts normalised with intensity due to intensity fluctuations as a function of the distance target-detector for the neutron region. This region is represented for 161 mm case in Fig. 27.

In the figures presented, Fig. 29, Fig. 30, and Fig. 31, there is no discernible tendency observed in the normalised number of counts as a function of the distances. Contrary to our expectations, described in the previous section (5.1.2), we anticipated that the counts of detected particles would decrease with increasing target-detector distance. However, we have to normalise the number of counts with the intensity which, in this case, was only measured at the end of each run, resulting in a direct impact on the behaviour of the detected counts.

Nevertheless, we can observe a meandering pattern in all three plots, which corresponds to the fluctuations in beam intensity. It is notable that, in the case of high-energy gamma rays and neutrons, Fig. 29 and Fig. 31, the fluctuation of the count numbers is directly proportional to the fluctuation of the beam intensity, represented in Fig. 32 (increased intensity corresponds to a higher number of counts). Conversely, for low-energy gamma rays, the relationship is inverted: the fluctuation of the count numbers is inversely proportional to the fluctuation of the beam intensity (higher beam intensity leads to a lower number of counts).

It is important to note that the measurement of 170 mm had to be redone due to a file-saving error, and it was conducted while measuring the odd distances between 171 mm and 169 mm. We can see in Tab. 9, the intensity for the three measurements is identical. This further reinforces the idea that the meandering observed in the count
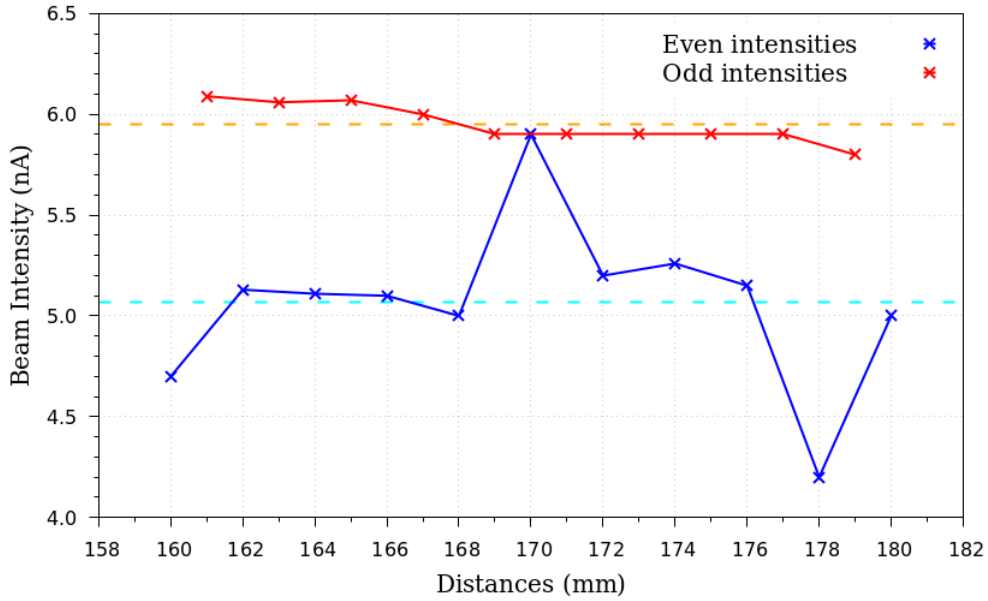
Fig. 32. Beam intensity as a function of the distance target-detector. We have represented the two set of measurements, odd and even distances, and have added the average value of the intensity of each set with a dashed line.

numbers is directly influenced by the fluctuations in intensity, particularly during the activation and deactivation of the beam. The staggering observed between beam current measurements makes us believe that there is an important systematic error most likely due to the positioning of the Faraday cup. This makes impossible to do a proper normalisation and may be the reason why we cannot find the smooth trend we were looking for.

In Fig. 32, we have plotted the intensity fluctuations as a function of the target-detector distances. The graph illustrates a range variation from 4.2 nA to 6.1 nA. These fluctuations arise from the necessity to turn off and on the beam each time we want to change the position of the target. Only at the end of each measurement were we able to assess the intensity. It is highly likely that the intensity also fluctuates throughout the duration of the measurement, and it is also very likely that the positioning of the Faraday outside cup varies between measurements. This process involves displacing the target to align the Faraday cup to the beam. Subsequently, once the target is realigned with the beam and set to the following positions, the beam is turned on again.

It is evident that the intensity values for even distances are around 5.07 nA and exhibit less stability, whereas the intensity values for odd distances are around 5.95 nA and demonstrate lower variability. To examine the impact of intensity on the count numbers, we can regard the intensities ranging from 5.9 nA to 6.07 nA as indicators of intensity stability, essentially, the odd distances set including 170 mm distance.
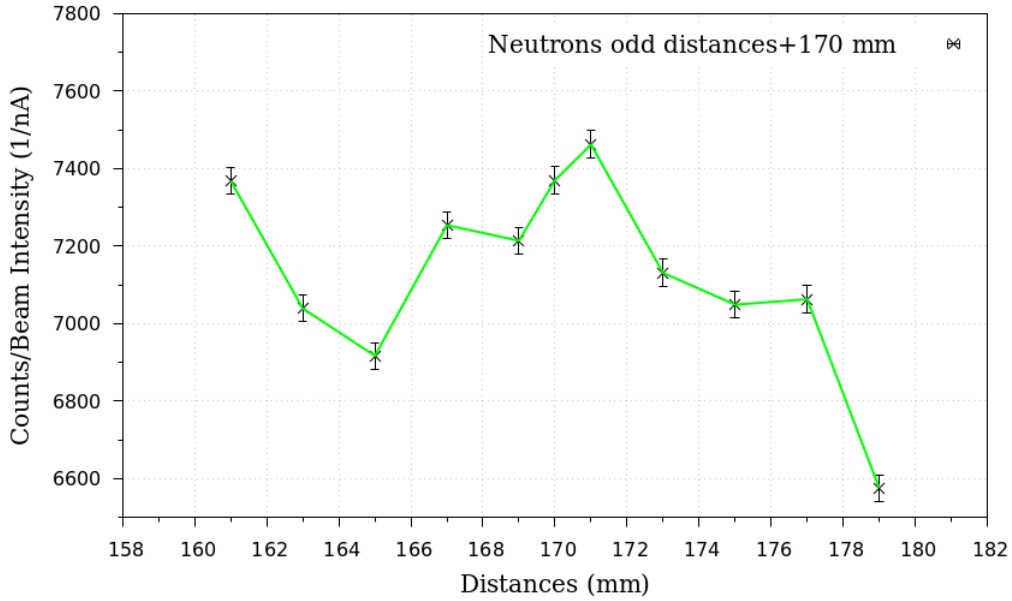
Fig. 33. Counts normalised with intensity due to intensity fluctuations as a function of the distance target-detector for the neutron region with the values corresponding to the odd set (adding 170 mm for the previously discussed reasons).

Based on Fig. 33, it appears that we cannot obtain a conclusive result that aligns with the simulations. The reason for this discrepancy is the inability to monitor the intensity during the measurement process, as we stated before. These variations in intensity can significantly impact the observed results and contribute to the inconclusive outcome when comparing with the simulations. For the second measurement at CMAM we designed a continuous monitoring of the beam intensity based on charge integration at the target.

5.2.2 Variation of the neutron flux with polyethylene

Additionally, we examined the impact of a polyethylene block as a moderator for fast neutrons generated by a 10 MeV proton beam colliding with a CsI target. We performed measurements at three distinct beam-detector distances: 165 mm, 170 mm, and 175 mm. Each measurement lasted 5 minutes, providing sufficient statistical data to facilitate a comprehensive comparison of the results.
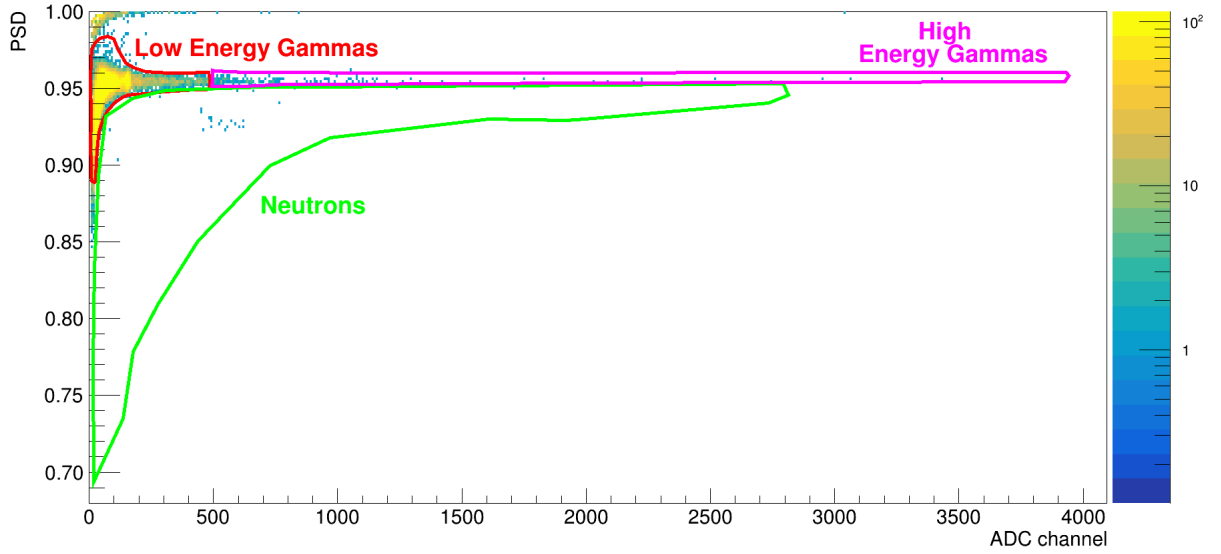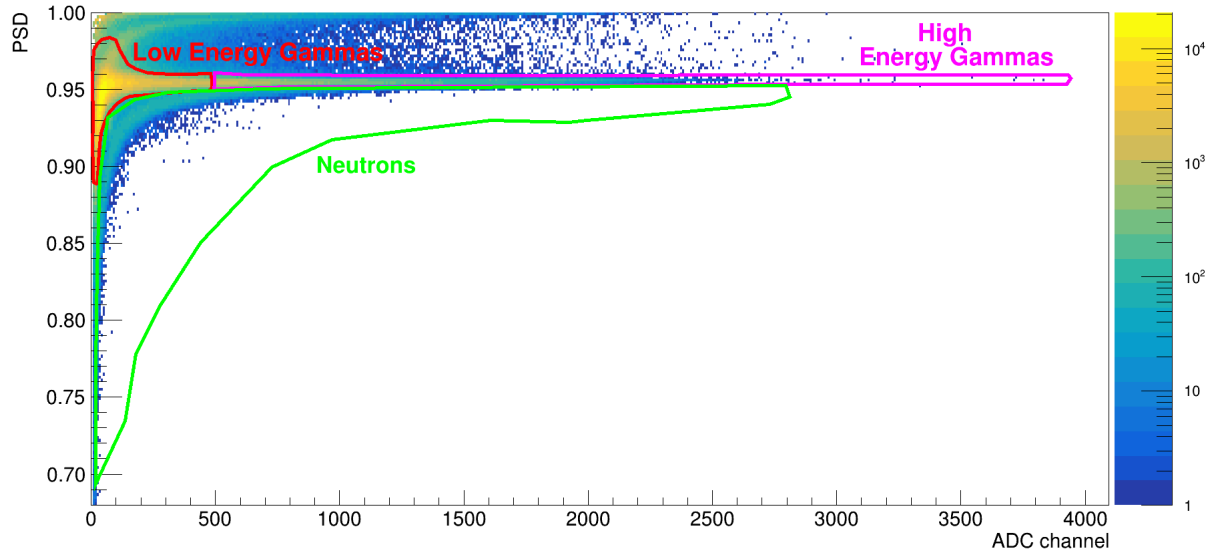
Fig. 34. PSD as a function of ADC channel for a background measurement with polyethylene in a distance of 175 mm.

Initially, a background measurement was conducted at a beam-detector distance of 175 mm, with a polyethylene block placed in front of the detector. The plot depicting the PSD versus ADC channel at the 175 mm position is presented in Fig. 34. It is evident that the neutron region exhibits very low counts. Comparing it with Fig. 35a, we observe that the low-energy gamma region also exhibits minimal counts in contrast to Fig. 35a. Nevertheless, the high-energy gamma region contains the majority of the counts. Consequently, we can attribute the bulk of high-energy gamma rays to background noise, including the contribution from the polyethylene block.

Fig. 35a illustrates the graphical divisions made to define the areas corresponding to high-energy gammas (pink), low-energy gammas (red), and neutrons (green). The neutrons region encompasses the α-particles and proton products generated by the (n,p) and (n,α) reactions.

Drawing a comparison between the results obtained with and without a block of polyethylene at the same position proves to be useful. Taking the PSD vs ADC channel plot at a distance of 170 mm as an illustrative example, we examine the case with polyethylene depicted in Fig. 35a, and the case without polyethylene shown in Fig. 35b. On visual inspection, no significant difference is discernible. However, to precisely determine the variance in counts, particularly for neutrons that undergo moderation with polyethylene, it is beneficial to compute the integral for each distinct graphical region. The discrepancy in counts has been compiled in Tab. 10.

45

(a) At 170 mm, with polyethylene.
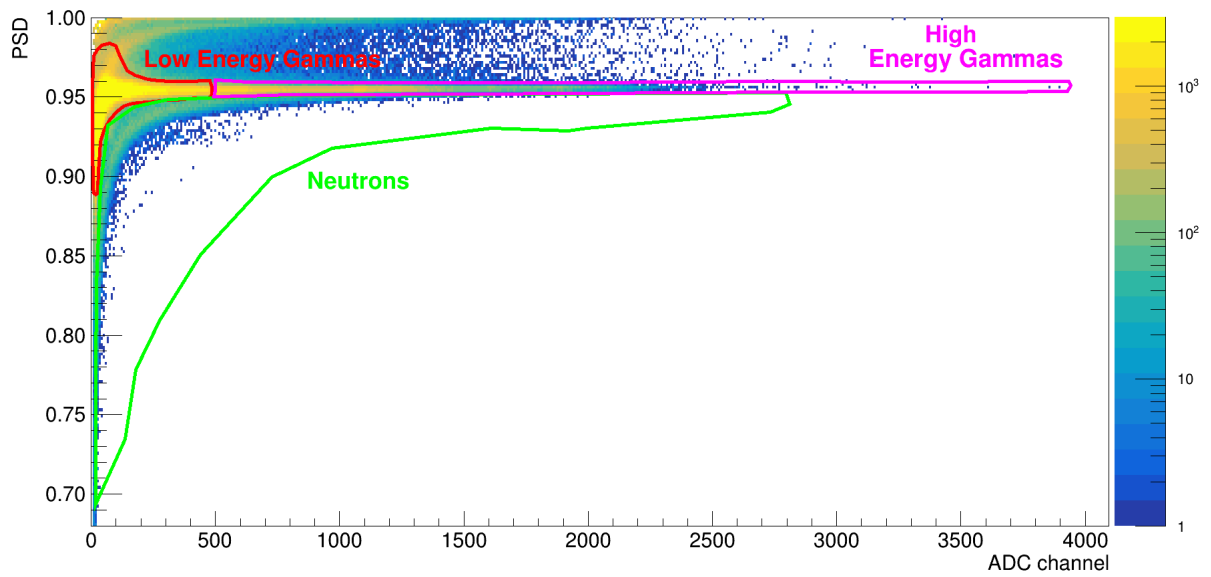
(b) At 170 mm, without polyethylene.

Fig. 35. PSD as a function of the ADC channel for a 5-minute measurement conducted at a distance of 170 mm, both with and without a 5 cm thick polyethylene block.

Normalised number of counts				
Type	Position (mm)	High-energy gammas	Low-energy gammas	Neutrons
Background with polyethylene	175	170 ± 13	38818 ± 197	30 ± 5
With Polyethylene	165	9156 ± 39	294481 ± 226	6283 ± 33
	170	9457 ± 40	305361 ± 230	6497 ± 33
	175	9345 ± 39	290326 ± 219	6244 ± 32
Without Polyethylene	165	24755 ± 64	286070 ± 225	6917 ± 34
	170	25183 ± 66	273349 ± 223	7370 ± 35
	175	24233 ± 64	263740 ± 220	7049 ± 35

Tab. 10. Numerical values representing the normalised number of counts obtained for measurements conducted with and without a polyethylene moderator at various beam-detector distances of 165 mm, 170 mm and 175 mm.
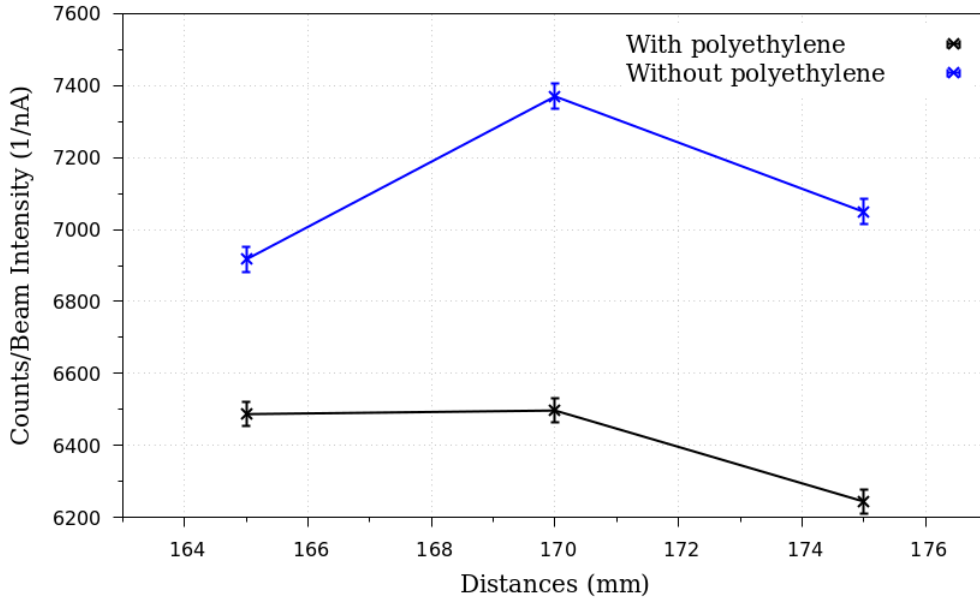

Fig. 36. Counts normalised with intensity due to intensity fluctuations as a function of the distance target-detector for the neutron region. We have represented the polyethylene and non polyethylene cases.

In Fig. 36, it is evident that neither the polyethylene nor the non polyethylene case exhibit a clear tendency. As stated before, this is due to the intensity fluctuations. Upon comparing the two cases, it becomes clear that the presence of the polyethylene moderator reduces considerably the number of counts since it slows down the neutrons and our crystal is especially efficient to detect fast neutrons. This is in good agreement to the Monte Carlo simulations of the previous section.

6 Conclusions

In conclusion, our study involved optimising the signal integration lengths and other acquisition configuration parameters to prepare the $LaCl_3$ detector to conduct CMAM measurements. We compared the figures of merit (FOM) obtained for the different PMTs, namely the R1924A-700 and R6233-100, using the same data acquisition parameters. Based on our analysis, we determined that the R1924A-700 was the most suitable PMT for conducting the measurements. However, due to concurrent experiments, we only had the R6233-100 available, which we used for our measurements.

Furthermore, we performed a simulation using a neutron beam and a $LaCl_3$ crystal detector, without simulating the reaction of a proton beam impacting a CsI target or the processing of the PMT. The simulation results aligned with our expectations, demonstrating that the $LaCl_3$ detector is capable of discriminating a 1 mm difference in distance. The agreement was observed across various energy ranges, including low-energy and high-energy gammas as well as neutrons. Notably, the number of counts detected increased with proximity to the neutron source, highlighting the influence of the solid angle effect.

Based on the experimental results of the CMAM measurements, conclusive results could not be obtained due to the unsuitability of the setup. Initially, we expected our results to align with the simulations; however, certain factors directly affected the outcomes. Specifically, the instability in beam intensity during the measurements and the need to turn the beam on and off to reposition the target significantly impacted the results. Beyond the instability itself, the fact that we did not have a direct measurement of this beam current during the measurements, only before and after each run, and they were always different. In a second experiment, beyond the scope of this master thesis, we could demonstrate that the system works very nicely when the beam is stable and we integrate the current on target.

Our analysis indicates that the behaviour of low-energy gammas and neutrons mirrors the fluctuations in beam intensity, while high-energy gammas demonstrate an opposite fluctuation pattern. By segregating the measurements into two distinct sets, odd distance values plus the 170 mm distance, and even distance values without 170 mm, we still observe a fluctuating pattern, even though with reduced intensity fluctuations. Nevertheless, it is important to note that despite our efforts, we still do not observe a consistent overall trend and the detector still does not display sensitivity to a 1 mm variation in distance.

In addition to the aforementioned effects of beam current instability on the measurements, we also observed that the presence of a polyethylene block further influenced the results. A comparative analysis conducted at identical distances, comparing measurements with and without the polyethylene block, highlighted the effectiveness of the moderator in

slowing down fast neutrons generated by the proton beam's interaction with the target. This implies that incorporating a moderator surrounding the detector in all directions except forward, serves as shielding for the neutrons scattered in in the walls of the hall that would normally contribute to the background.

In conclusion, our study indicates that the $LaCl_3$ detector, when used in an intensity-variable facility, does not yield reliable results for neutron-gamma discrimination with 1 mm increments. The analysis revealed limitations and challenges associated with the intensity fluctuations and other factors that directly affected the detector's performance.

7 Next-steps

We are currently conducting a second test in CMAM using the PMT R1924A-700 and a ^{241}Am/^{9}Be source to investigate PSD discrimination in the $LaCl_3$ scintillator. In this second phase of the project, we could differentiate between protons, alphas, and gammas at a high voltage (HV) of -1100 V, as explained in the previously study. The ^{241}Am emits alphas that are captured by ^{9}Be, resulting in the emission of neutrons through the ^{9}Be$(\alpha, n)^{12}$C reaction. We were able to continuously monitor the beam intensity using a current integrator connected to the target, which addressed the intensity fluctuations encountered in the previous CMAM experiment. The results of this second measurement are promising. Although it was beyond the scope of this thesis, I had the opportunity to participate in this experiment.

To replicate the conditions of proton range verification in proton therapy, a third phase of the project would involve studying the variation of the position of the Bragg peak in a proton therapy facility. It is crucial to achieve better control over intensity fluctuations and overcome issues related to stopping and restarting the neutron emission in order to test the scintillator under real-life conditions. This would help determine its potential application in proton therapy.

8 References

[1] R. P. Johnson, "Review of medical radiography and tomography with proton beams," *Reports on progress in physics* **81** no. 1, (2017) 016701.

[2] V. Giacometti, "Modelling and improvement of proton computed tomography,".

[3] F. Hueso-González and T. Bortfeld, "Compact method for proton range verification based on coaxial prompt gamma-ray monitoring: A theoretical study," *IEEE transactions on radiation and plasma medical sciences* **4** no. 2, (2019) 170–183.

[4] D. Chattopadhyay, S. Sharma, and M. S. Sarkar, "Elimination of the effect of internal activity in lacl3: Ce scintillator," *Journal of Instrumentation* **16** no. 06, (2021) P06025.

[5] P. Q. Vuong, H. Kim, N. T. Luan, and S. Kim, "Neutron spectroscopy using pure $LaCl_3$ crystal and the dependence of pulse shape discrimination on ce-doped concentrations," *Nuclear Engineering and Technology* **53** no. 11, (2021) 3784–3789.

[6] F. Crespi, F. Camera, *et al.*, "Alpha–gamma discrimination by pulse shape in labr3: Ce and lacl3: Ce," *Nuclear Instruments and Methods in Physics Research Section A: Accelerators, Spectrometers, Detectors and Associated Equipment* **602** no. 2, (2009) 520–524.

[7] C. Hoel, L. Sobotka, K. Shah, and J. Glodo, "Pulse-shape discrimination of la halide scintillators," *Nuclear Instruments and Methods in Physics Research Section A: Accelerators, Spectrometers, Detectors and Associated Equipment* **540** no. 1, (2005) 205–208.

[8] A. Pankratenko, T. Kormilitsyn, Y. A. Kashuck, S. Y. Obudovsky, D. Fridrikhsen, A. Shevelev, E. Khilkevitch, M. Iliasova, N. Bakharev, and O. Skrekel, "Analysis of the lacl3 (ce) scintillator response function to fast neutrons," *Nuclear Instruments and Methods in Physics Research Section A: Accelerators, Spectrometers, Detectors and Associated Equipment* **1052** (2023) 168282.

[9] J. A. Briz, A. Nerio, *et al.*, "Proton radiographs using position-sensitive silicon detectors and high-resolution scintillators," *IEEE Transactions on Nuclear Science* **69** no. 4, (2022) 696–702.

[10] S. Agostinelli, J. Allison, *et al.*, "Geant4—a simulation toolkit," *Nuclear instruments and methods in physics research section A: Accelerators, Spectrometers, Detectors and Associated Equipment* **506** no. 3, (2003) 250–303.

[11] https://www.nndc.bnl.gov/nudat3/.

[12] L. Farabee, "The removal of alpha-contamination from lanthanum by ion exchange," *US AEC, TID-7591* (1960) 78–80.

[13] B. D. Milbrath, R. C. Runkle, T. W. Hossbach, W. R. Kaye, E. A. Lepel, B. S. McDonald, and L. E. Smith, "Characterization of alpha contamination in lanthanum trichloride scintillators using coincidence measurements," *Nuclear Instruments and Methods in Physics Research Section A: Accelerators, Spectrometers, Detectors and Associated Equipment* **547** no. 2-3, (2005) 504–510.

[14] https://www.caen.it/products/dpp-psd/.